*J. Fluid Mech.* (2010), *vol.* 649, *pp.* 467–496.  
doi:10.1017/S0022112009993971

# An experimental study of turbulent vortex rings during their early development

L. GAN† AND T. B. NICKELS

Department of Engineering, Cambridge University, Trumpington Street, Cambridge CB2 1PZ, UK

(Received 27 September 2009; revised 11 December 2009; accepted 11 December 2009)

In this paper, the early development of turbulent vortex rings at two Reynolds numbers is studied using two-dimensional and stereoscopic particle image velocimetry (PIV). In the late 1980s, a similarity theory of turbulent vortex rings was proposed and this theory was tested primarily using laser Doppler velocimetry (LDV). However, because of limitations of the experimental technique, the tests were inconclusive and important assumptions could not be checked. Because single-point measurements were used, vortex ring structures could only be inferred using a complex signal analysis technique. In this study, the PIV technique provides spatial measurements of the full field of the cross-section of a ring from which a more rigorous investigation of the similarity theory is possible. Because the region over which the similarity theory appears to hold starts at about 2.5 orifice diameters downstream, this study focusses on the early development region from this point to 8 diameters downstream. Finally, Reynolds stresses and turbulence production contours are presented. The effects of ring dispersion on the measurements is also studied and quantified.

## 1. Introduction

A vortex ring in laboratory study is usually generated by the impulsive ejection of fluid through a nozzle or an orifice into a quiescent environment. The inner boundary layer of the nozzle or the orifice is ejected and rolls up to form a toroidal structure, which is known as a vortex ring. The velocity and the stroke length of the piston motion determine the circulation of the vortex ring and may be used to define a Reynolds number which partly characterizes the nature of the ring (Lim & Nickels 1995).

$$Re = \frac{\Gamma_0}{\nu} = \frac{U_p L}{2\nu}, \tag{1.1}$$

where $U_p$ is the velocity of the piston downstroke and $L$ is the piston stroke length. When this Reynolds number is sufficiently high (or the stroke length is sufficiently long), the nature of the ring is observed to be unsteady, complex and three-dimensional: these rings are referred to as turbulent vortex rings. Note that Glezer (1988) has mapped out the conditions under which vortex rings will be laminar, laminar becoming turbulent later, and turbulent from the outset.

Detailed quantitative data at various downstream locations from the nozzle exit for various stages of rings' development history have been given by many researchers but mostly for laminar or relatively low-Reynolds-number cases, among which are Maxworthy (1977) and Didden (1979). There have been relatively few studies of

† Email address for correspondence: lg331@cam.ac.uk

turbulent vortex rings, such as Maxworthy (1974), Johnson (1971) and Sallet & Widmayer (1974). The most comprehensive study of turbulent vortex ring structure, however, is given by Glezer & Coles (1990), in which a long-term similarity solution was proposed based on the assumption of the invariance of the impulse and experiments were made to examine the ring's structure and turbulence statistics.

LDV was used in this study, which only provided instantaneous velocity information at a single point in flow field. This limitation is important since spatial structure must be inferred from temporal information. This is why Glezer & Coles (1990) developed a profound signature recognition scheme to filter out imperfect or suspicious data points and applied time-axis shifting before applying conventional statistical methods to obtain ensemble-averaged structures. A similarity theory based on the invariance of the hydrodynamic impulse was then proposed which, together with the use of Taylor's hypothesis, allowed the researchers to calculate turbulence statistics for a turbulent vortex ring. The similarity theory is based on the dimensional analysis and it was shown that turbulent vortex rings follow similar development from as early as 2.5 nozzle (orifice) diameters downstream from the exit. This study, while careful and comprehensive, suffered from a number of limitations (that were recognized and noted by the authors) which includes:

(i) Spatial structure is inferred using Taylor's hypothesis from single-point measurements.

(ii) Only two components of the velocity were measured for the ring.

(iii) Ring dispersion was significant and difficult to correct for when relying on point measurements. (The term dispersion is not clearly defined by Glezer & Coles (1990). It is a general term to indicate the location difference of the ring cores from one instantaneous realization to another. In this paper, this term refers to the distance from the instantaneous ring core locations from that of the ensemble-averaged ring.)

(iv) The invariance of the impulse was assumed but could not be checked.

In this report, two-dimensional and stereoscopic PIV techniques are used to capture the spatial structure of turbulent vortex rings for their early lives (first 8 diameters) and some of the limitations described above are overcome.

## 2. Experimental methodology

### 2.1. *Apparatus*

This experiment is conducted in a tank of water of dimensions $750 \times 750 \times 1500$ mm in the Cambridge University Engineering Department. Vortex rings are generated by an impulsive vertical movement of a piston mounted on the top of the tank. The $\varnothing$144 mm diameter piston is driven by a stepper motor (SmartDrive Ltd.), which is controlled by a programmable controller (Taranis). The velocity profile of the piston movement is controlled by programming in BASIC language and the piston can move up to 1000 mm $s^{-1}$ with an acceleration and deceleration of about 1500 mm $s^{-2}$. The diameter of the piston/nozzle system was designed previously for large ring studies. In order to study the longer distance/time range of rings while maintaining reasonable spatial resolution, a small orifice of $\varnothing$50 mm is cut in the centre of a horizontal plate, mounted over the cylinder exit, and two cameras are lined-up vertically to cover a large field of view (FOV) with a common overlapped FOV of about $1D$. Experiments are carried out for two Reynolds numbers (different by a factor of two) in order to investigate the possible dependence of structural differences on Reynolds number. The $Re$ for the vortex rings is calculated by converting the piston speed and the stroke length to those effectively for smaller orifice. For the first condition, the

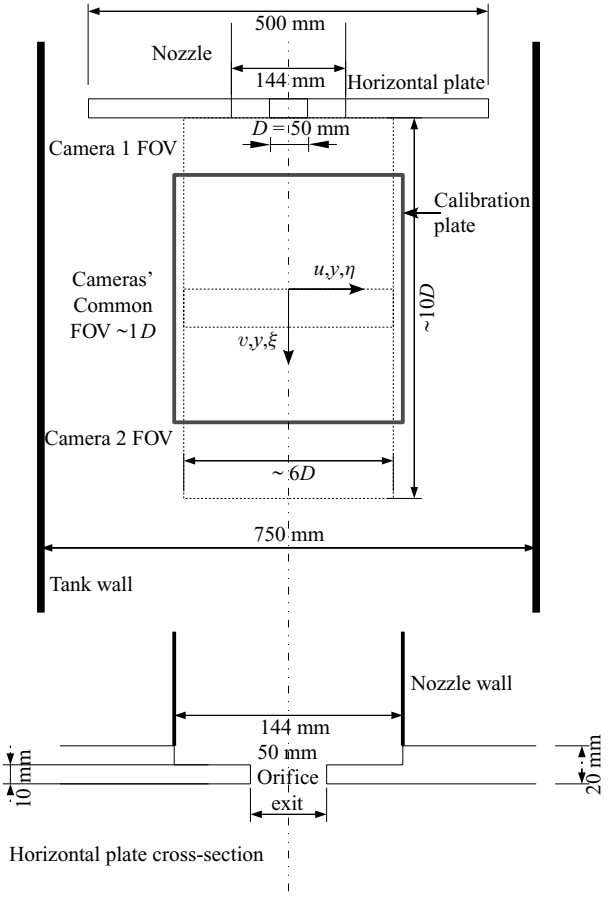


FIGURE 1. Schematic diagram of the testing section in the centre section of the tank (piston and motor not shown) and the centre section of the horizontal plate. The diagram is not in scale.

effective $Re_1$ is set to 41 280 in order to match the one of Glezer & Coles (1990) and since the starting point of the similarity theory (which is about $2.5D$ downstream of the nozzle exit, Glezer & Coles 1990) is of interest, $y/D$ is limited to 8 (where $y$ is the downstream distance measured from the orifice exit); for the second condition, the FOV is increased to about $10D$ and the effective $Re_2$ is set to 20 039. In both cases, $y$ is limited to the top half of the tank to eliminate the boundary effect from the tank bottom. The experimental set-up is summarized schematically in figure 1. The PIV system was provided by LaVision and uses two Photron APX cameras. The cameras are capable of running at a frame rate of 500 Hz with 4 s recording time which provides a fairly good temporal resolution and duration. The cross-correlation interrogation window size and overlap size are set to $16 \times 16$ pixels and 25 % to give a spatial resolution of 2.48 mm for the $Re_1$ case and 3.15 mm for the $Re_2$ case. Note that this resolution in comparison with the ring diameter is similar to that of Glezer & Coles (1990) using LDV. There are $85 \times 85$ data points in one camera's resultant vector mesh. The effective $L/D$ ratio for the small orifice for both cases is 3.43. For each case, 50 realizations are produced to obtain reasonable statistical convergence; see figure 3. The quantity computed in figure 3 is effectively the convergence speed of the

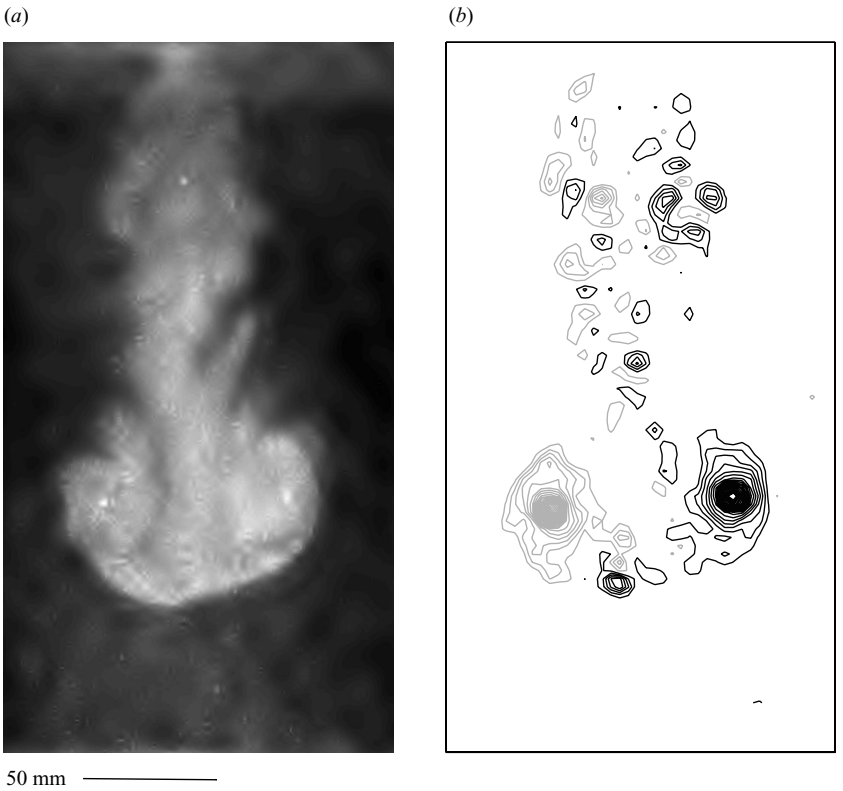


FIGURE 2. (*a*) Flow visualization of ring's centre cross-section, using a denoized image of extremely high particle density at $Re = 20\,039$; (*b*) the corresponding vorticity field. Contour levels are $-110.0(5.0)-5.0$ and $5.0(5.0)110.0\ \mathrm{s}^{-1}$.

turbulent stresses:

$$\tau_N = \frac{1}{N}\sum_{i=1}^{N}\left[(u_i - \overline{u_N})^2 + (v_i - \overline{v_N})^2\right], \tag{2.1}$$

where $\overline{u_N} = (1/N)\sum_{i=1}^{N} u_i$, $\overline{v_N} = (1/N)\sum_{i=1}^{N} v_i$ and $u$, $v$ are the radial and axial velocity component, respectively, as defined in figure 1. The convergence testing points for both $Re$ cases are put in the core centre region, where the maximum turbulent stress intensities occur (see figures 16 and 17); therefore, stresses converge most slowly. Although the transition map of Glezer (1988) indicates that at the condition of $Re \cong 20\,000$ combined with $L/D \cong 3.5$, the rings are in transition zone from laminar to turbulent, figure 2 suggests that the rings are already quite turbulent.

### 2.2. *Theoretical background*

In this section, we follow closely the analysis of Glezer & Coles (1990), though note the difference in the coordinates. On the basis of the dimensional analysis given by Glezer & Coles (1990), the streamfunction of a vortex ring can be fully described by its hydrodynamic impulse $I$, the density of the fluid $\rho$ and the kinematic viscosity $\nu$:

$$\psi = f(I, \rho, \nu) = g(y, r, t), \tag{2.2}$$

where $y$ and $r$ are in cylindrical coordinates, $r$ is the axis in the radius direction from the axis of symmetry, $y$ is the axis in the streamwise direction from the orifice exit,

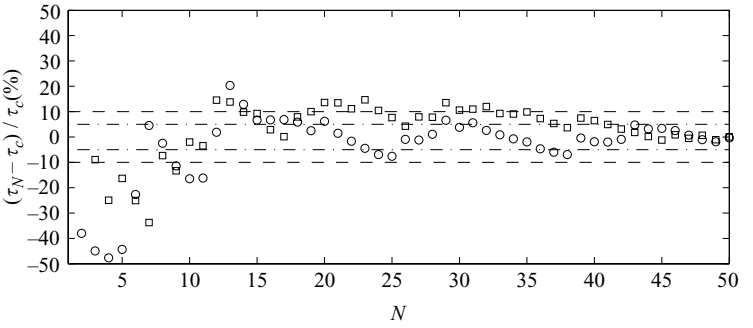


FIGURE 3. Convergence testing for the number of realizations needed for each $Re$ case. The term $\tau_N$ is defined in (2.1); $\tau_c = \tau_{50}$. The testing point's position is about $0.1D$ outside the left core centroid (quite in the core centre region) for both $Re$ cases where the rings are at $5.5D$ downstream from the exit. Symbols: ○, $Re_1 = 41\,280$ case; □, $Re_2 = 20\,039$ case. Lines: ——, $\pm 10\,\%$; — · —, $\pm 5\,\%$.

$t$ is the time from the beginning of the piston movement. In Cartesian coordinates, $r$ is equivalent to $(x - x_o)$, where $x_o$ is the centre of the flow field, the mean ring centre trajectory. The coordinate system adopted in this study is defined in figure 1. Hydrodynamic impulse hence can be written as

$$\boldsymbol{I} = \frac{1}{2}\rho \int_{\boldsymbol{V}} (r \times \omega)\, \mathrm{d}\boldsymbol{V}, \tag{2.3}$$

where $\omega$ is the vorticity and $\boldsymbol{V}$ is the entire fluid volume.

If the Reynolds number is sufficiently high and the flow is highly turbulent, the dependence of the stream function on the kinematic viscosity can be neglected, leaving only the other two quantities to govern the flow equation. Before the energy of the vortex ring dies out significantly, the ring is still considered highly excited and turbulent. Mathematically, when the circulation $\Gamma$ has not decayed significantly, the ratio $\Gamma/\nu$ is still large and the effect of the kinematic viscosity is still considered negligible, $\nu$ can be dropped from (2.2). This is also one of the reasons why this experiment is limited to the early development of turbulent vortex rings: at large times viscous decay and cross-annihilation of vorticity will become important. While the similarity transformation does not strictly require the invariance of the impulse (the local value could be used from a dimensional perspective), it is this assumption that leads to specific predictions for the variation of the other quantities of interest. As a result, it is difficult to directly test for similarity without making this assumption. Maxworthy (1974) observed that the vortical structure is continuously shed from the main ring to the wake and concluded that the similarity transformation of the ring is not possible. Glezer & Coles (1990), however, argued that if the hydrodynamic impulse is considered as the total mechanical impulse of the non-conservative body force required to generate the velocity field from zero, and if the entire unbounded flow field is considered instead of just the main ring itself, this quantity should be considered as invariant. It will be shown in § 3.1 that, even though the entire flow field is being considered, the hydrodynamic impulse $I$ is not quite constant. In fact, a later study showed that the hydrodynamic impulse is not equivalent to mechanical impulse, and this point will also be further commented on in § 3.1. If the invariance

of the hydrodynamic impulse $I$ is accepted, (2.2) can be rewritten as

$$\psi t^{1/4}\left(\frac{\rho}{I}\right)^{3/4} = f_2\left(y\left(\frac{\rho}{It}\right)^{1/4}, r\left(\frac{\rho}{It}\right)^{1/4}\right). \tag{2.4}$$

With a proper pair of spatial and temporal virtual origins defined $(y_o, t_o)$, (2.4) can be written as

$$S = \psi\,(t - t_o)^{1/4}\left(\frac{\rho}{I}\right)^{3/4} = S\,(\xi, \eta)\,, \tag{2.5}$$

where $S$ is the dimensionless streamfunction, $\xi$, $\eta$ are the dimensionless quantities for the axial and radial coordinates $y$ and $r$, respectively:

$$\xi = (y - y_o)\left(\frac{\rho}{I\,(t - t_o)}\right)^{1/4}, \quad \eta = r\left(\frac{\rho}{I\,(t - t_o)}\right)^{1/4} \tag{2.6}$$

and

$$U = u\left(\frac{\rho}{I}\right)^{1/4}(t - t_o)^{3/4}, \quad V = v\left(\frac{\rho}{I}\right)^{1/4}(t - t_o)^{3/4}, \tag{2.7}$$

where $u$, $v$ are the radial and axial velocity component, respectively, as defined in figure 1; $U$, $V$ are the corresponding dimensionless quantities.

Hence, the following set of rules must be satisfied if the rings obey the similarity property (and the impulse is invariant):

(*a*) $r \sim (y - y_o)$.
(*b*) $(y - y_o)^4 \sim (t - t_o)$.
(*c*) $v^{-1/3} \sim (t - t_o)^{-1/2} \sim (y - y_o)$.

## 3. Results and discussion

### 3.1. *The similarity property*

The simplest test of similarity is to consider the variation of the ring radius as a function of streamwise distance. This is shown in figure 4. The ring size is determined by locating the centroids of both cores and each core is defined by the area which is enclosed by a closed contour of 40 % of the peak vorticity. Note that at $L/D \cong 3.5$, formation wake phenomena appear (Gharib, Rambod & Sharrif 1998) and because of the highly turbulent nature of the rings, vorticity is continuously shed from the ring bubble area. There are two points worth emphasizing here:

(*a*) Gharib *et al.* (1998) indicated that the formation wake starts to be visible at about $L/D \cong 4(3.6 - 4.5)$, nevertheless in this experiment, at $L/D = 3.43$, significant formation wake is already observed. Two reasons may be responsible for the shorter formation time: firstly, more energetic or stronger vortices can advance the formation time more rapidly (Dabiri 2009); secondly, a different ring generator configuration is used in this experiment.

(*b*) The detailed vorticity shedding manner deserves a further study, Weigand & Gharib (1994) observed a stepwise shedding in a much lower $Re$ ring and for a relatively long time duration. A preliminary study of vorticity shedding in individual $Re = 20\,039$ rings indicates a different manner from stepwise shedding during their early lives. It is possible that up to the end of the testing time, stepwise shedding has not started yet.

To minimize the error in determining the centroids, the wake is excluded when determining the core area. It is worth noting that individual realizations are also very important in the study of turbulent vortex rings, because the inevitable dispersion

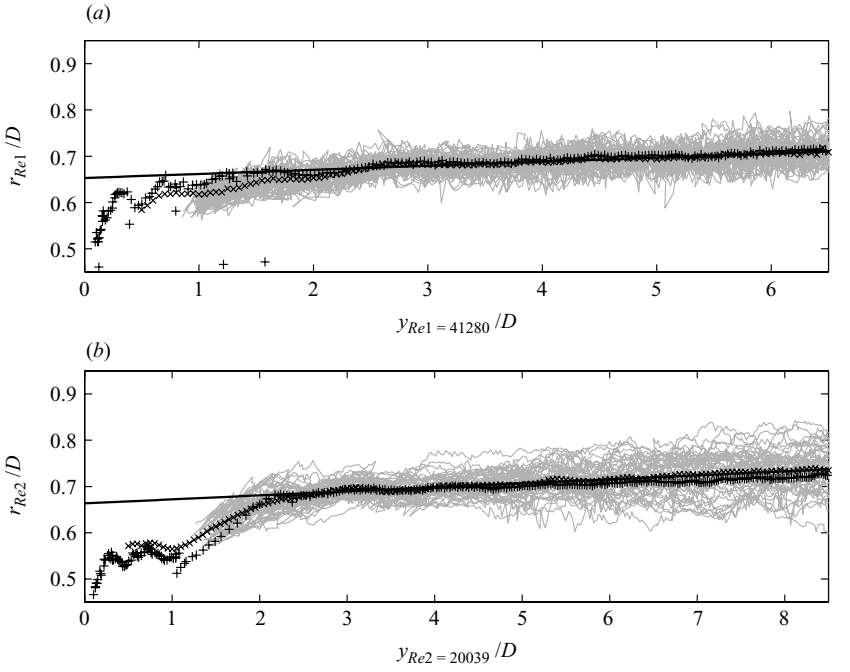


FIGURE 4. Ring radius $r$ as a function of downstream distance $y$ for both Reynolds numbers. The grey lines are the traces of each of the 50 realizations; $\times$ denotes the ensemble-averaged radius based on location; $+$ denotes the ensemble-averaged radius based on arrival time; $-$denotes the first-order least square fit of $\times$ starting from $y/D = 3.5$.

in core position and geometry tends to smear out actual behaviour. It is for this reason that each of the 50 individual realizations is plotted (grey lines). Moreover, because the $y$ axis is the downstream position, it is more sensible to ensemble average quantities based on location. The entire FOV is divided into a number of stations along the streamwise direction starting from the orifice exit. The distance between neighbouring stations is $0.05D$. All the 50 realizations are ensemble averaged when the apparent centre of the ring (judged from the locations of the two core centroids) reaches each station, regardless of the arrival time (the difference is quite small, which will be indicated later). As can be seen, compared with the result of averaging based on arrival time, this fits the individual trace zone (grey zone) better especially at early times. A first-order least square fit is applied after $3.5D$ downstream from the orifice exit from which the virtual origins can be determined which are $-74.32D$ for the $Re_1$ case and $-76.37D$ for the $Re_2$ case. Furthermore, from the slopes of these fitting lines, the growth rates (cone angles) can also be estimated, which are 0.0176 and 0.0174, respectively. These numbers are comparable with the results of the early researchers, which are listed in table 3 of Glezer & Coles (1990). The agreement with the early research results is one reason why this plot is used to determine the virtual origin. Note the different approaches to determine the ring radius in this study as compared with some of the early research where flow visualization was used. Core vorticity centroids are not always located at the rotating centre of a passive scalar, especially for turbulent cores where the vorticity contour is not always regularly circular; hence, the growth rate here is slightly different from the flow visualization results. Individual traces for $Re_2$ are obviously more scattered. The reason is that a turbulent vortex ring

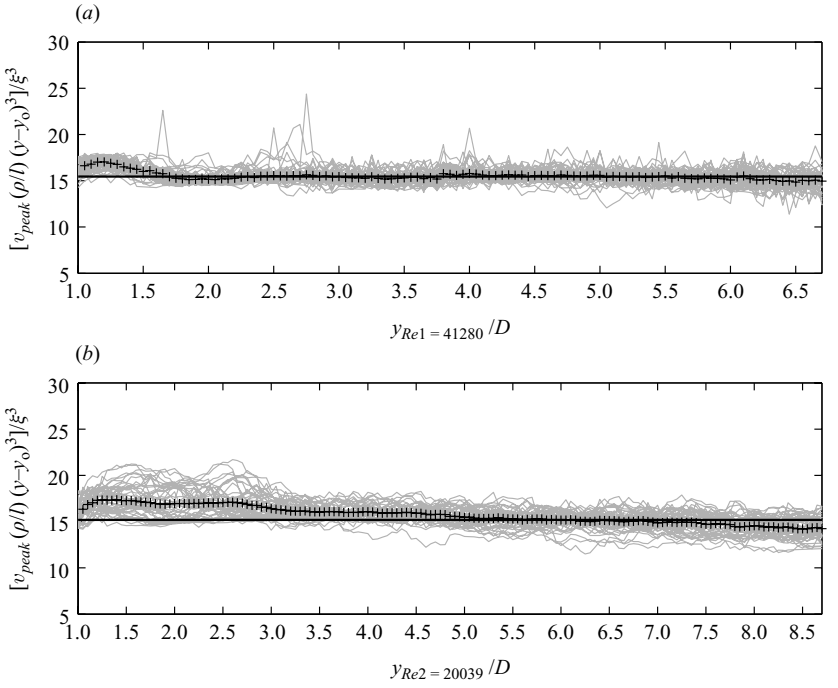


FIGURE 5. Peak axial velocity $v_{peak}$ on the ring centre trajectory as a function of downstream distance. Velocity is scaled accordingly to similarity theory. Grey lines are the traces of each of 50 realizations; + is the ensemble-averaged value from individual realizations; — is the zero-order least square fit of + after $y/D = 3.5$, which represents the similarity theory. Here $y_o$ is obtained from figure 4.

may have an azimuthal wave-like instability (similar to that analysed by Widnall & Tsai 1977 for laminar rings). For the lower $Re$ case, the rings navigate slower so the waves may have bigger amplitudes at the same streamwise location. This situation makes the core centroids look scattered more severely in the PIV plane. Because of their turbulent nature, the shed vorticity from the core along the azimuthal direction is highly unlikely to be uniform, the consequence of which is the uneven distribution of local circulation along the azimuthal direction, causing the ring to tilt and disperse from the mean trajectory. These are important properties of turbulent vortex rings, hence one cannot apply an artificial treatment such that the cores appear exactly on top of each other. This point is discussed in § 3.2.

The virtual origins just estimated are used to determine other similarity quantities (so the same virtual origins are used for all quantities). Firstly, the peak velocity in the field of interest (FOI) is plotted against streamwise distance in figure 5. The peak velocity, which is in the axial direction, is located on the centre of the ring trajectory. Both plots show that similarity theory weakly underestimates the decay of the peak velocity. (In this paper, when quantities are plotted as a function of the ring's streamwise distance, if they are scaled according to similarity theory, they are expected to be constant.) The disagreement is less clear in the $Re_1$ case, where it is only noticeable at the last few points, but it is reasonable to anticipate that the deviation will grow farther downstream. It is worth emphasizing that this is the plot which Glezer & Coles (1990) used to determine the virtual origin. If a free first-order

least square fit is applied to $v_{peak}^{-1/3}$ against $y$ plot, it would indicate an unreasonably large angle of growth when compared with the earlier results.

Interestingly, the similarity theory seems to predict the ring navigation speed or celerity quite well. If (2.6) is differentiated, the equation for navigation speed can be obtained. The strong noise at the beginning is due to the incomplete formation process: the main ring has not pinched off yet.

If the ring navigation velocity is subtracted from the velocity field, the resultant velocity field will be that of an observer moving at the same velocity as the ring. Assuming that the ring is completely isolated, two stagnation points can be found with one located at the windward tip and the other at the leeward tip. Because of the existence of a wake only the windward stagnation point is easily recognized but that is enough to determine the stagnation streamline which forms an open ellipse. With the approximation that the bubble is an axisymmetric oblate spheroid, it is possible to compute the volume of the bubble by numerical integration. In order to locate the windward stagnation point more precisely, the original data point mesh is firstly refined by a factor of 10 using two-dimensional cubic spline interpolation, after which this refined mesh is also used to increase the accuracy of the numerical integration scheme. The scaled ring volume as a function of streamwise distance is plotted in figure 7. It can be observed that the two data sets obey the similarity theory quite well after $3.5D$. There is a subtle waviness in the two data sets, indicating an oscillation of the ring bubble: the reason for this is left for future study. It may be related to vorticity shedding from the core area or it may be related to the waviness on the core changing the imaged cross-sectional area (and hence the inferred volume).

Fluid entrainment fractions for vortex rings can also be computed from the ring bubble volumes. The entrainment fraction is defined in the same way as defined by Dabiri & Gharib (2004) for the purpose of comparing the quantity to that of the laminar rings.

$$\kappa(t) = \frac{\Omega_{bubble}(t) - \Omega_{ejected}(t)}{\Omega_{bubble}(t)} = 1 - \frac{\Omega_{ejected}(t)}{\Omega_{bubble}(t)}, \tag{3.1}$$

where $\kappa$ is the entrainment fraction, $\Omega_{bubble}$ is the ring bubble volume, $\Omega_{ejected}$ is the total volume of the fluid ejected from the orifice during the formation process and all the three quantities are functions of time. In contrast to the laminar rings of comparable $L/D$ value in Dabiri & Gharib (2004), which indicate an entrainment fraction of about 0.3, figure 8 shows two major differences: firstly, the entrainment fraction is negative, meaning that the ring bubble volume is smaller than the fluid volume ejected from the piston nozzle, in which the formation wake should be responsible to the missing part; secondly, the laminar ring shows a fairly constant entrainment fraction as a function of time while entrainment fractions in figure 8 increase with time with slopes of 0.050 and 0.033 for $Re_1$ and $Re_2$, respectively. Note that the bubble volumes of turbulent rings at two Reynolds numbers are similar at same downstream distances as shown in figure 7 but $Re = 41\,280$ rings navigate much faster than $Re = 20\,039$ rings, the ratio of their celerities can be calculated from figure 6.

As mentioned above, vorticity is continuously shed from the ring bubble volume to the wake and it is in the wake where most cancellation and annihilation of opposite-signed vorticity takes place. This mechanism causes the circulation of the ring bubble area and the entire FOV to decrease. The plot of the circulation is presented in figure 9, which has been scaled according to the similarity scaling law. The theory underestimates the decay of the bubble circulation by a very small factor

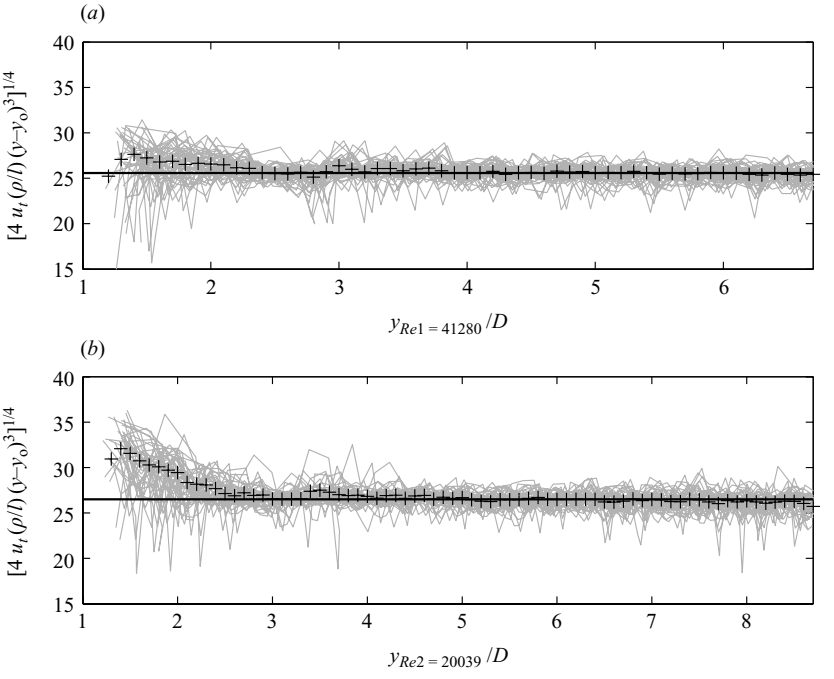


FIGURE 6. Ring navigation speed, celerity $u_t$ scaled according to similarity theory. The dimensionless quantity $\xi$ is determined from this plot, which is the quantity on the vertical axis; the dimensionless celerity $U_t = (1/4)\,\xi$. Grey lines are the traces of each of the 50 realizations; + is the ensemble-averaged value from individual realizations; − is the zero-order least-square fit of + after $y/D = 3.5$, which represents the similarity theory. Here $y_o$ is obtained from figure 4.

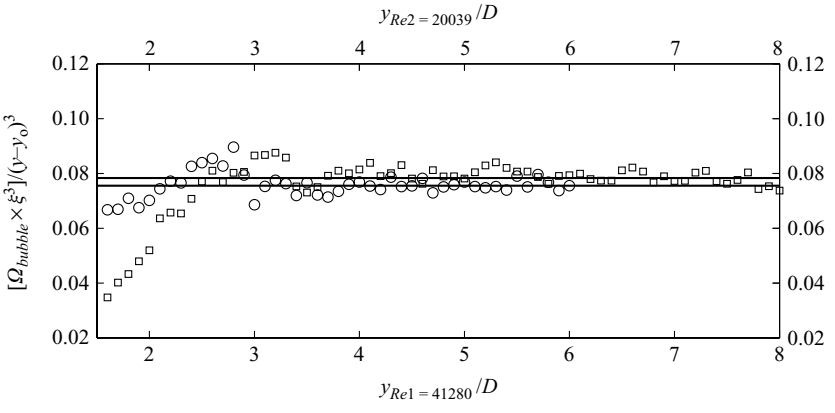


FIGURE 7. Ring bubble volume $\Omega_{bubble} = 2\times\int_{y_a}^{y_b}\pi r^2(y)\,\mathrm{d}y$ as a function of downstream distance calculated from the ensemble-averaged velocity field, where $y_a$ is the windward stagnation point and $y_b$ is the point at the maximum radius; $r(y)$ is determined by the stagnation streamlines. Symbols: ○, $Re_1$ case; □, $Re_2$ case. The volume is scaled according to the similarity theory. Note that − is the zero-order least-square fit after $y/D = 3.5$, which represents the similarity theory. Here $y_o$ is obtained from figure 4.

up to the extent of the FOV. It is not very clear in the $Re_1$ case, but downstream there is a small deviation. While the circulation of the bubble decays roughly in line with the similarity theory, the circulation of the entire field decays much more

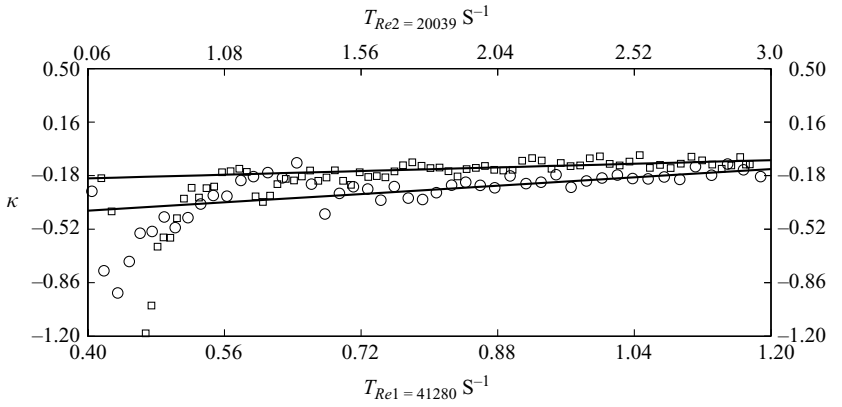


FIGURE 8. The entrainment fraction $\kappa$ as a function of time calculated from the ensemble-averaged velocity field. Symbols: ○, $Re_1$ case; □, $Re_2$ case. Here — is the first-order least-square fit after 0.72 s and 1.56 s for $Re_1$ and $Re_2$ cases, respectively.

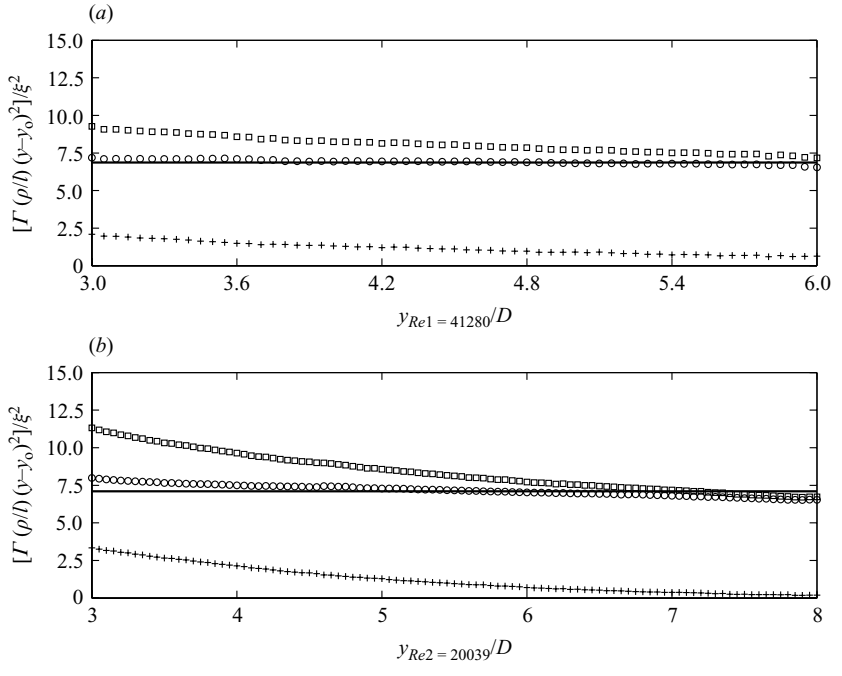


FIGURE 9. Circulation as a function of streamwise distance computed from $\Gamma_{B'} = \int_{B'} \omega \, dx \, dy$, based on the ensemble-averaged vorticity contours for both $Re$ cases. Symbols: □, the whole flow field, where $B'$ represents left/right half of the entire flow fields; ○, the ring bubble area, where $B'$ represents the rectangular region of $1.4D$ in the streamwise direction and $1.2D$ in the radial direction aside on the ring's mean trajectory; +, the wake part, simply is the difference between □ and ○. The circulations of the ring bubble area are scaled by similarity law in which the two — are the zero-order least-square fits after $y/D = 3.5$ with $y_o$ obtained from figure 4.

rapidly. This may be predominantly due to annihilation of vorticity in the wake. Although vorticity leaving the PIV plane due to three-dimensional effects may also be responsible, because there is a weak anisotropy in the wake part, this effect is

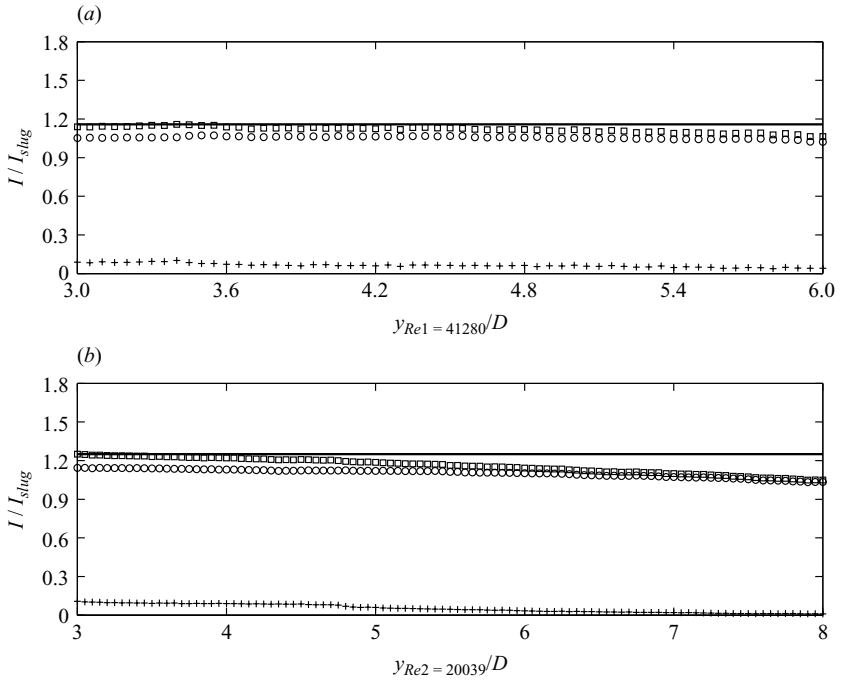


FIGURE 10. Hydrodynamic impulse as a function of streamwise distance computed from (2.3), based on the ensemble-averaged vorticity contours for both $Re$ cases. The quantity is normalized by slug impulse. Symbols: □, the whole flow field; ○, the ring bubble area which is simplified as a rectangular region of $1.4D$ in the streamwise direction and $2.4D$ in the radial direction; +, the wake part, simply is the difference between □ and ○; −, the maximum impulse level of the whole flow field.

not believed to be as important as the annihilation effect. Farther downstream, the amount of vorticity obtained from shedding from the ring bubble is not enough to compensate for that being continuously annihilated in the wake. The vorticity shedding process only involves the lowest level around the ring cores, therefore the effect is less significant.

The variation of the hydrodynamic impulse as a function of streamwise distance is also presented in figure 10 in an attempt to show how the decay of the circulation is related to the behaviour of the impulse. A small decay is observed in the bubble impulse which agrees with Maxworthy (1974), as well as the full field impulse, although it is much less severe than the decay of the full field circulation. The amount of decay of the full-field impulse up to the last points in figure 10 is about 8 % and 16 % for the $Re_1$ and $Re_2$ cases, respectively, and the decay of the bubble impulse is about 5 % and 10 % respectively (note the different end points for the two cases). On the one hand, the increase of the ring radius (see figure 4) leads to an increase in impulse (see (2.3)); on the other hand, the vortical structures shed from the bubble are less intense, and hence result in only a small loss of the ring impulse. The slug model underestimates both impulse and circulation (Didden 1979; Lim & Nickels 1995 and Shariff & Leonard 1992). It is noteworthy that the impulse responsible in the similarity theory is the hydrodynamic impulse which is computed from (2.3). Saffman (1992) derived the impulse required to set a region of fluid into an unsteady vortical motion that includes an extra term, which is not always easy to measure empirically.

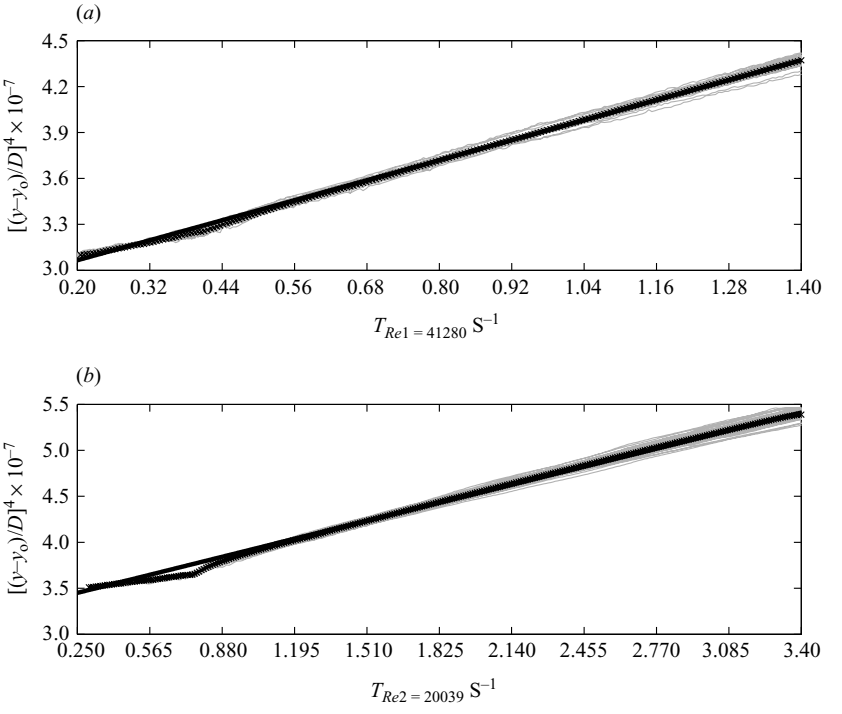


FIGURE 11. Determination of the virtual time origins by intersecting the line to the time axis. Grey lines are the traces of each of 50 realizations.

This impulse is written as

$$\boldsymbol{I} = \frac{1}{2}\rho \int_v (r \times \omega)\, \mathrm{d}\boldsymbol{V} + \rho \int_s \phi \boldsymbol{n}\, \mathrm{d}\boldsymbol{S}, \tag{3.2}$$

where $\boldsymbol{n}$ is the unit normal vector directed into the region of compact vorticity, and $\phi$ is the velocity potential at the surface $\boldsymbol{S}$ of the body. Notwithstanding the dominance of the first term in many circumstances – hence it is often used by itself for force estimation – the second term can be substantial sometimes (Krueger & Gharib 2003).

Finally, the virtual time origins of both cases can be determined by plotting the ring locations against arrival times as is shown in figure 11. The two virtual time origins are $-2.61$ s and $-5.28$ s for $Re_1$ and $Re_2$ cases, respectively.

### 3.2. *The raw turbulence quantities*

If the similarity theory is believed to work, at least over some distance for both Reynolds number cases, the velocity components can be scaled according to (2.7). In order to verify the validity of the scaling law, testing ranges are set from $4D$ to $6D$ for the $Re_1$ case and $5.5D$ to $7.5D$ for the $Re_2$ case such that rings are located as far downstream as possible while the whole ring structure can still be seen. Velocity components at each station within the testing ranges are then scaled. Figure 12 shows that the scaling law works well and curves of both Reynolds number collapse very well, indicating that Reynolds number is not a strong factor influencing the mean velocity. Mean velocity and vorticity contours are presented in figures 13–15. It is worth noting that, even though figure 5 indicates that the similarity theory does not work perfectly for the entire data range presented, for the range tested, the theory

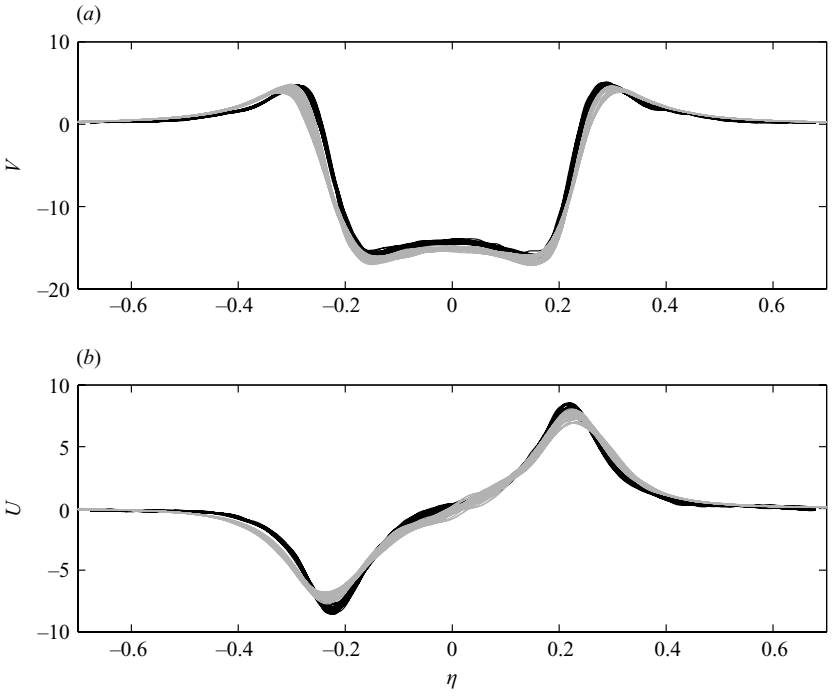


FIGURE 12. Velocity components at all the testing stations scaled by similarity theory for two Reynolds number cases. The axial component is chosen to cut the two core centres (at each station locations); the radial component is chosen to be $0.1D$ below the core centre, simply because this quantity vanishes across the centres. Black traces: $Re_1 = 41\,280$; grey traces: $Re_2 = 20\,039$.

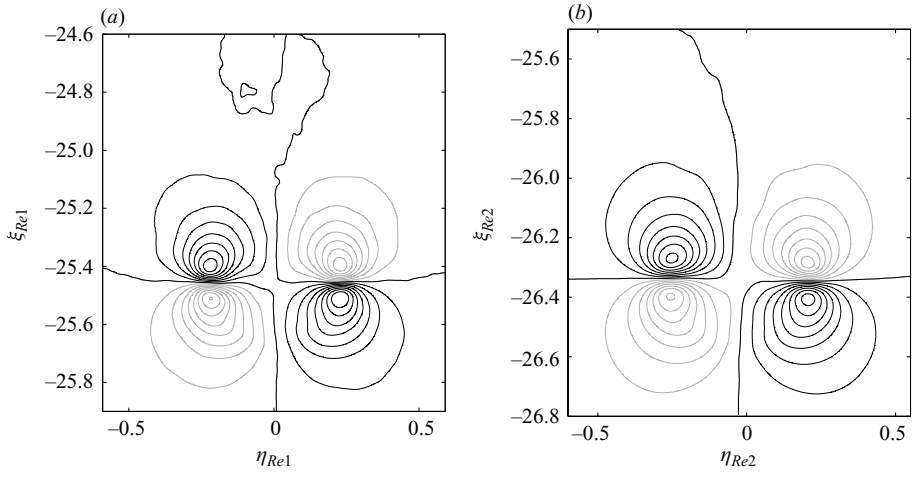


FIGURE 13. Radial velocity $U$ contour in similarity coordinates. Contour level is $-8.0(1.0)8.0$.

works well. The time scale involved in (2.7) is set to be the averaged arrival time of 50 rings at the station being tested. The largest arrival time difference at a station is typically below $\pm 0.15$ s, which is negligible when the value of $t_o$ is considered.

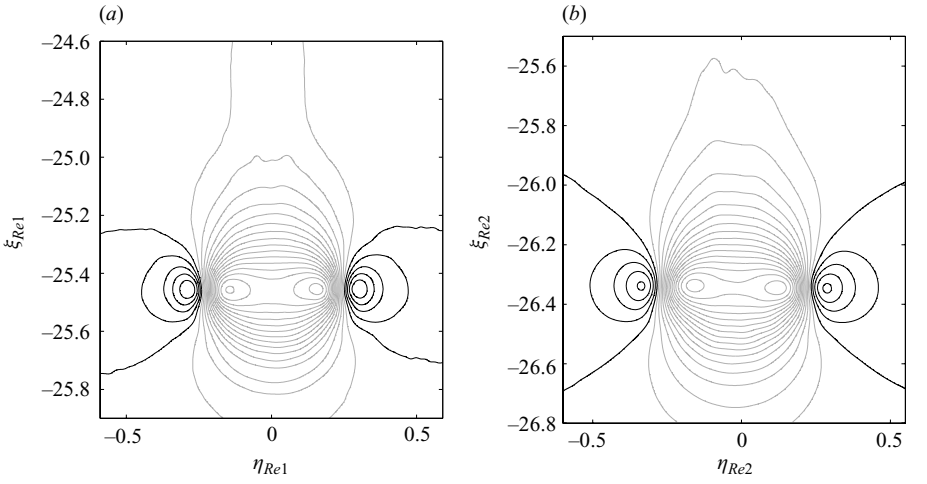


FIGURE 14. Axial velocity $V$ contour in similarity coordinates. Contour level is $-16.0(1.0)5.0$.

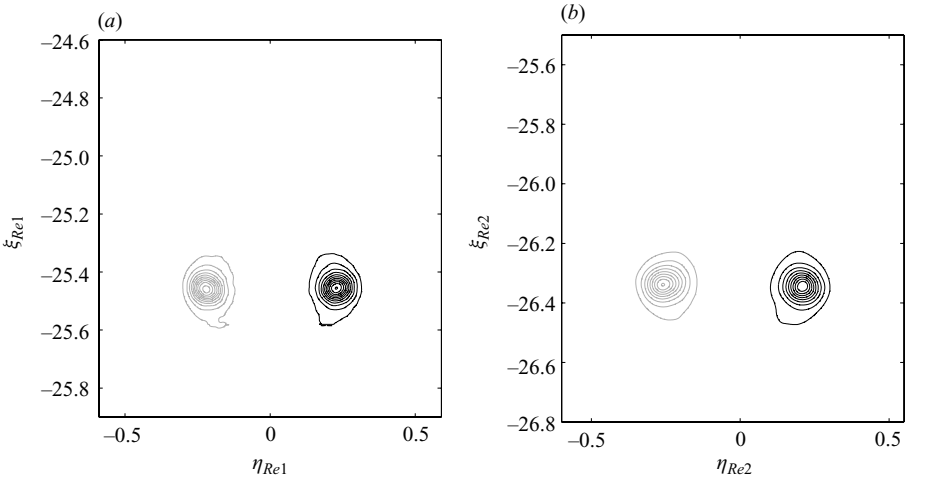


FIGURE 15. Vorticity $\partial V/\partial\eta - \partial U/\partial\xi$ contour in similarity coordinates, obtained from velocity contours. Contour levels are $-600(50)50$ and $50(50)600$.

In order to better understand the turbulence structure, it is necessary to examine the turbulence stresses and production. Because the mean structure appears to follow similarity well, turbulence quantities here are scaled using the similarity transformation (The relationships between the real quantities and the similarity quantities can be deduced from (2.7), and they are not illustrated here.) and they are presented in similarity coordinates from figures 16–18 and 21 for rings of both Reynolds numbers. Peak turbulence quantities can be clearly identified and the positions are located very close to the mean vortex cores. When comparing these structures with the LDV results, perhaps the most distinguished difference is the degree of asymmetry, which is partly due to the different experimental approaches. Note that the results presented by Glezer & Coles (1990) are perfectly symmetrical since they measured only one side and reflected for presentation in the contour plots. This small asymmetry also exposes the most important contributor of the turbulence quantities, dispersion, reasons for which have been discussed in § 3.1. The second obvious difference, perhaps, is the existence

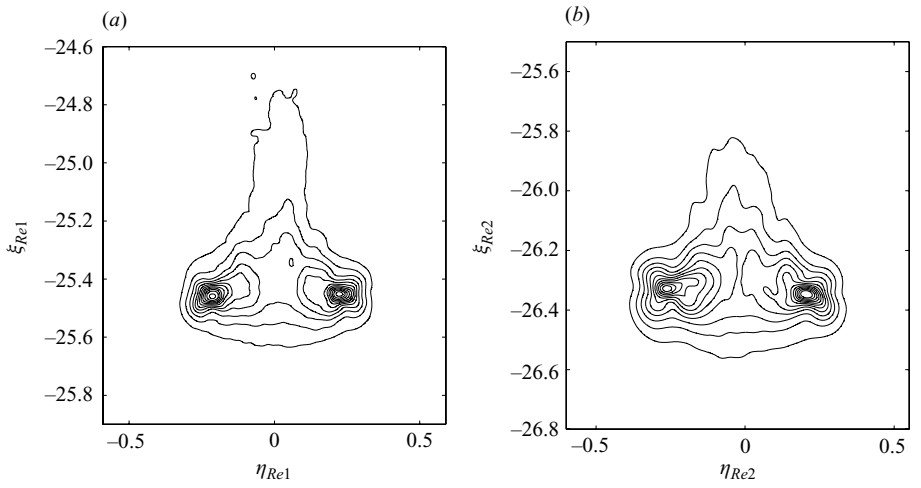


FIGURE 16. Radial normal Reynolds stresses $-\overline{U'U'}$ contour in similarity coordinates. Contour level is −12.0(1.0)1.0. Higher levels in the core centre area are not shown.

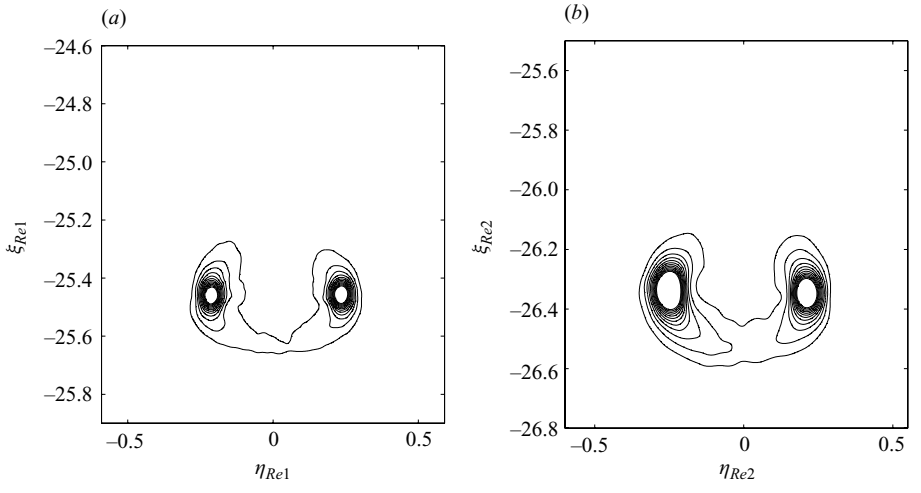


FIGURE 17. Axial normal Reynolds stresses $-\overline{V'V'}$ contour in similarity coordinates. Contour level is −24.0(2.0)2.0. Higher levels in the core centre area are not shown.

of secondary cores beside main cores shown in LDV results of Glezer & Coles (1990), which seems only be possible when rings are located exactly at the same location and are of the same size and shape. This difference will be further discussed in § 3.3. Because the core centroids have a random scatter in the centroid cluster plot (not shown here), small details near the core centre (if they exist) will be smoothed away by the averaging process. In order to examine how dispersion affects the stress level and distribution, the core dispersion level is plotted in figure 20. Note that the effect of dispersion is to add to the turbulence intensities since it adds an extra effective fluctuation. This plot is able to explain several facts: firstly, the $Re_1$ case has a more symmetrical dispersion; therefore, stresses and production contours are more symmetrical for the $Re_1$ case; secondly, the left core dispersion is more severe in the $Re_2$ plot, which directly causes the intensities of the left core to exceed that of the right core in figure 17 for the $Re_2$

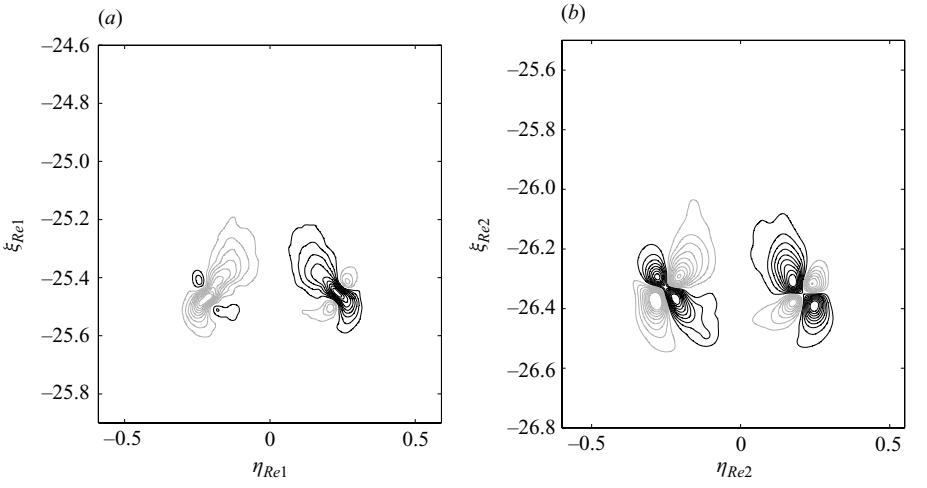


FIGURE 18. Reynolds shear stresses $-\overline{U'V'}$ contour in similarity coordinates. Contour level is −4.5(0.5)4.5. Higher levels in the core centre area are not shown.

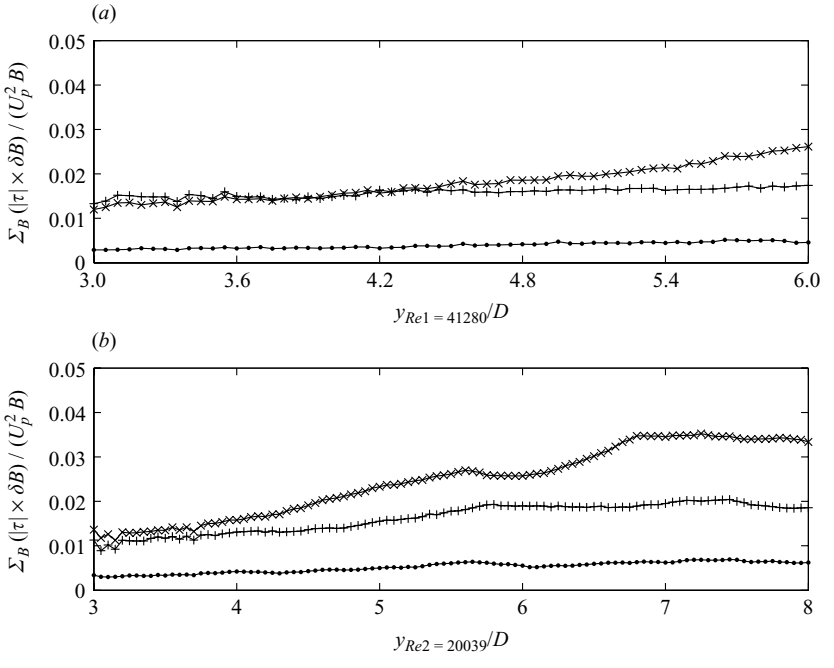


FIGURE 19. The summation of the magnitude of the three Reynolds stresses $\tau$: $-\overline{u'u'}$, $-\overline{v'v'}$ and $-\overline{u'v'}$ in the ring bubble area $\int_B |\tau| \, \mathrm{d}\boldsymbol{B}/U_p^2 B$ as a function of rings' streamwise locations. $B$ is the bubble region. In order to exclude the effect of the wake, the three overall stress levels are only computed in the ring bubble area. For simplicity, the bubble area is chosen to be a rectangular region of $1.4D$ in the streamwise direction and $2.4D$ in the radial direction, which is big enough to include the bubble but small enough to exclude the wake. This integrand is approximately equal to the integrand over the bubble area, since the stress level outside the bubble area is insignificant and hence negligible. This rectangular region is adopted for both cases and in all the similar calculations below. Referring to figure 7, the bubble volume of the two $Re$ cases only differs less than 10 %. Symbols: +, axial normal Reynolds stress; ×, radial normal Reynolds stress; ●, Reynolds shear stress.

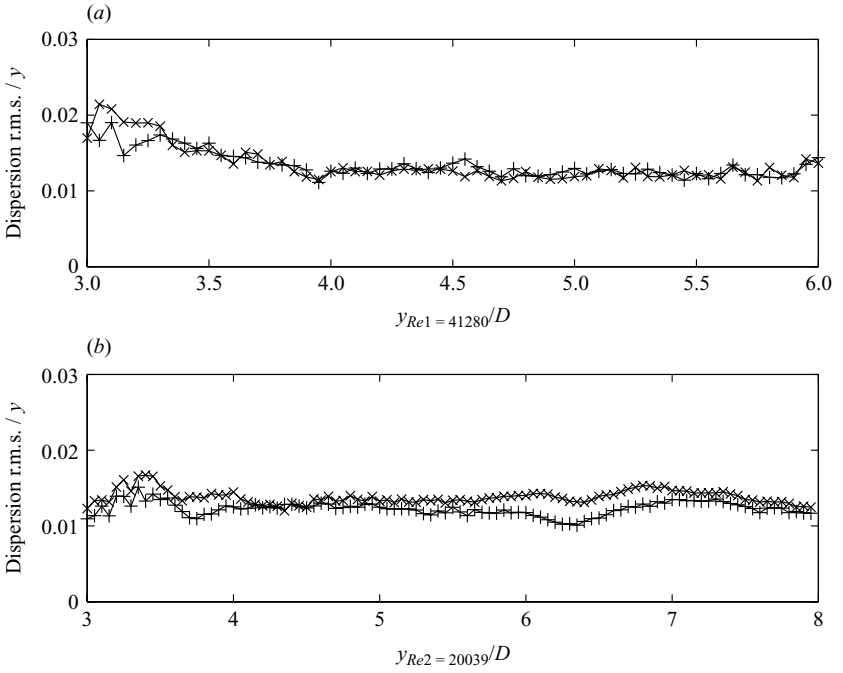


FIGURE 20. The r.m.s. of the apparent core centroids dispersion with respect to the mean core centroid streamwise location, $\sqrt{(1/N)\,\Sigma_N[(x_c-\overline{x_c})^2+(y_c-\overline{y_c})^2]}$, where $N=50$, $\overline{x_c}$ and $\overline{y_c}$ are the ensemble-averaged core location coordinates, $x_c$ and $y_c$ are the instantaneous core location coordinates of single realization. This quantity is normalized by the rings' streamwise location. Therefore, a flat line indicates an increased dispersion level. Symbols: $\times$, left core; $+$, right core.

case; thirdly, dispersion increases as the ring moves downstream, which may be the reason why the turbulence intensity level does not decay (shown in figure 19), while as predicted by the similarity theory, stress level at every point will decrease as $t^{-3/2}$ or $y^{-6}$; hence, the level of the stress integrated over the bubble area will decrease as $t^{-1}$ or $y^{-4}$. Despite the differences, general agreement with the broad features noted by Glezer & Coles (1990) is apparent, for instance, a wake can only be observed in the radial component of the normal stresses, not in the axial component.

The turbulence production is thought to be mainly due to the large scales; hence, it can be estimated (whereas the authors believe that the spatial resolution is not sufficient to calculate the dissipation in these measurements – so this will not be attempted). In two-dimensional Cartesian coordinates, turbulence production can be written as

$$p=-\overline{u_i'u_j'}e_{ij}=-\sum_{i=1}^{3}\sum_{j=1}^{3}\left(\frac{1}{2}\overline{u_i'u_j'}\frac{\partial\overline{u_i}}{\partial x_j}+\frac{1}{2}\overline{u_i'u_j'}\frac{\partial\overline{u_j}}{\partial x_i}\right), \tag{3.3}$$

where $\overline{u_i}$, $\overline{u_j}$ are mean velocities and $u_i'$, $u_j'$ are velocity fluctuations, $e_{ij}$ is the strain-rate tensor for the mean velocities. The subscripts of the above equation can only go up to 2 because of the lack of information of the third component using two-dimensional PIV recording. The two-dimensional production contour is presented in figure 21.

In an attempt to investigate components in the third direction, stereoscopic PIV measurements were made to provide the planar information of out-of-plane velocity component, such that the subscripts are able to be raised to three for some terms

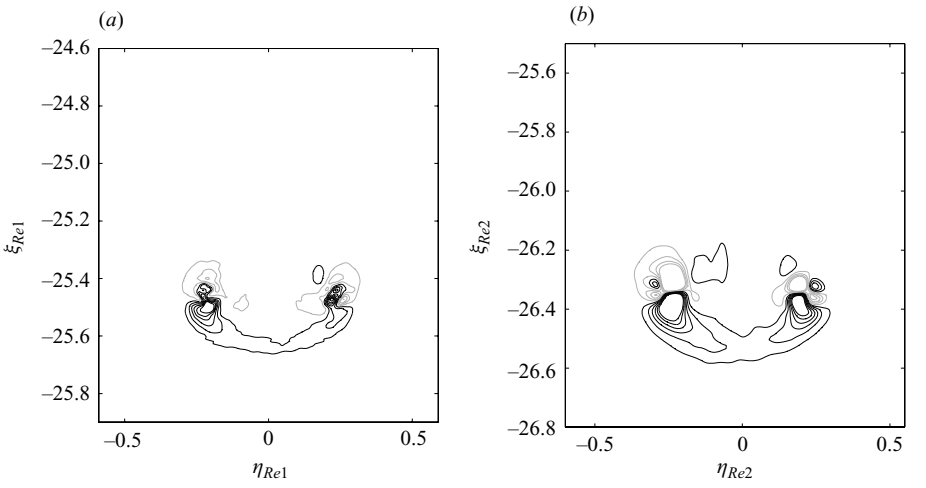


FIGURE 21. Turbulence production contour in similarity coordinates. Only the first four terms in (3.4) are included. Contour levels are −350(100)−50 and 50(100)550. Higher levels in the core centre area are not shown.

in (3.3). Thus among nine terms for the production, seven can be determined ($\partial w/\partial z = 0 - (\partial u/\partial x + \partial v/\partial y)$ by continuity, leaving only $\partial u/\partial z$ and $\partial v/\partial z$ undetermined). It should be noted that in the case that the ensemble average is considered to be axisymmetric, these extra terms will make no contribution. The centre of the measurement station for stereoscopic PIV recording is at 224 mm ($4.48D$) downstream from the orifice exit, the FOV covers about $2.5D$ in the streamwise direction and the spacial resolution is 2.15 mm. Stereoscopic measurements have only been made for the $Re_1 = 41\,280$ case. Equation (2.7) is also used to scale the true velocity into similarity velocities $U$ and $V$ for stereo results (In the third component, the relationship is similar as $U$ and $\eta$, named them $W$ and $\zeta$.) such that similarity scaled production $P$ becomes

$$P = \left(-\overline{U'U'}\frac{\partial \overline{U}}{\partial \eta}\right) + \left(-\overline{U'V'}\frac{\partial \overline{U}}{\partial \xi}\right) + \left(-\overline{U'V'}\frac{\partial \overline{V}}{\partial \eta}\right) + \left(-\overline{V'V'}\frac{\partial \overline{V}}{\partial \xi}\right) + \left(-\overline{W'W'}\frac{\partial \overline{W}}{\partial \zeta}\right) + \left(-\overline{U'W'}\frac{\partial \overline{W}}{\partial \eta}\right) + \left(-\overline{V'W'}\frac{\partial \overline{W}}{\partial \xi}\right). \quad (3.4)$$

Figures 22–24 show that most of the turbulence production is contained in the $x$–$y$ plane, the contribution from the out-of-plane components is generally weak except for the one which comes from the normal stress. Reynolds stresses obtained from stereoscopic recording are also presented in figures 25 and 26 as a comparison with figures 16–18. For Reynolds normal stresses, $-\overline{W'W'}$ component is comparable with $-\overline{U'U'}$ but is about half of the $-\overline{V'V'}$. The non-negligibility of the out-of-plane component occurs for two main reasons: firstly, the rings are strongly three-dimensional and are possibly dispersed in a direction with a component perpendicular to the PIV plane; secondly, possibly there exist significant azimuthal velocities along the core region (Maxworthy 1977). The main contribution to the Reynolds shear stress comes from components in the PIV measurement plane. To further prove the existence and importance of the $-\overline{W'W'}$ stress component, a different stereoscopic set-up is adopted. In this arrangement, PIV plane is positioned in parallel with the ring's azimuthal direction and is located at $6D$ downstream from the orifice exit.

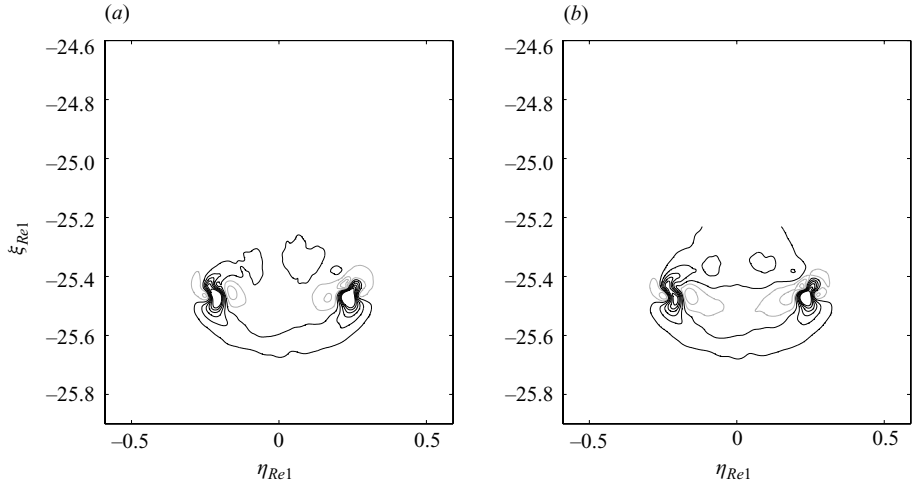


FIGURE 22. Part of the turbulence production in similarity coordinates. Contour levels are −350(100)−50 and 50(100)550. Higher levels in the core centre area are not shown. (*b*) is calculated from all seven terms in (3.4), and (*a*) is produced using the first four terms aiming to show the effect of the third components to the resultant contour. Note that the core centre locations are conserved in similarity coordinates, despite the independent experimental set-up.

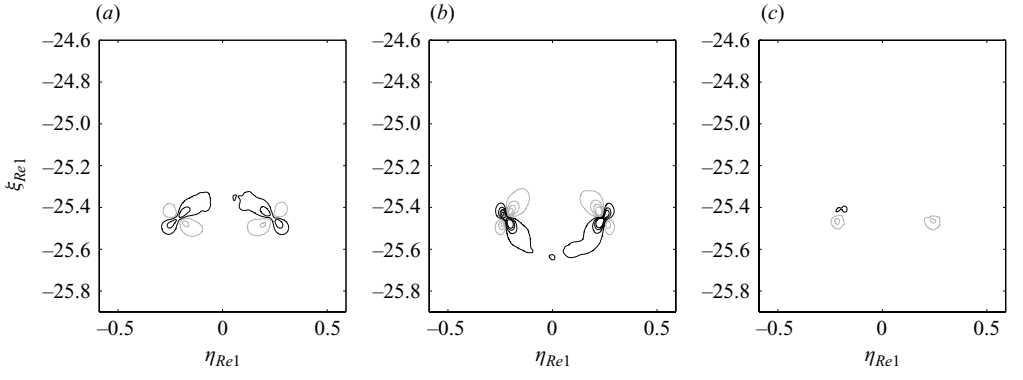


FIGURE 23. Part of the turbulence production, normal components (*a–c*): $-\overline{U'U'}\partial\overline{U}/\partial\eta$, $-\overline{V'V'}\partial\overline{V}/\partial\xi$, $-\overline{W'W'}\partial\overline{W}/\partial\zeta$ in similarity coordinates. Contour levels are −700(200)−100 and 100(200)700. Higher levels in the core centre area are not shown.

(Because of physical space restrictions, smaller streamwise locations are difficult to measure.) The spatial resolution in this set-up is 1.69 mm and only $Re_1 = 41\,280$ rings are studied. The three instantaneous velocity components are presented in figure 27 and in similarity coordinates. Although these are not Reynolds stresses, the strong three-dimensional structure is clearly observed and the importance of $-\overline{W'W'}$ is expected. The Reynolds stresses and other statistical quantities obtained from this experimental set-up are left for future studies.

### 3.3. *Turbulence quantities with some artificial corrections*

Since it is believed that dispersion makes a significant contribution to the total turbulent stresses, it is logical to attempt to decompose the total Reynolds stresses

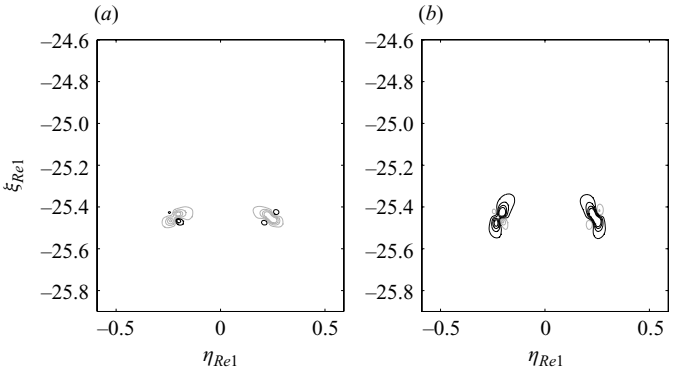


FIGURE 24. Part of the turbulence production, shear components (*a*,*b*): $-\overline{U'V'}\partial\overline{U}/\partial\xi$, $-\overline{U'V'}\partial\overline{V}/\partial\eta$ in similarity coordinates. Contour levels are −700(200)−100 and 100(200)700. Higher levels in the core centre area are not shown. Note that $-\overline{V'W'}\partial\overline{W}/\partial\xi$ and $-\overline{U'W'}\partial\overline{W}/\partial\eta$ are not shown because their intensities are too low, about 5 % those of the others.

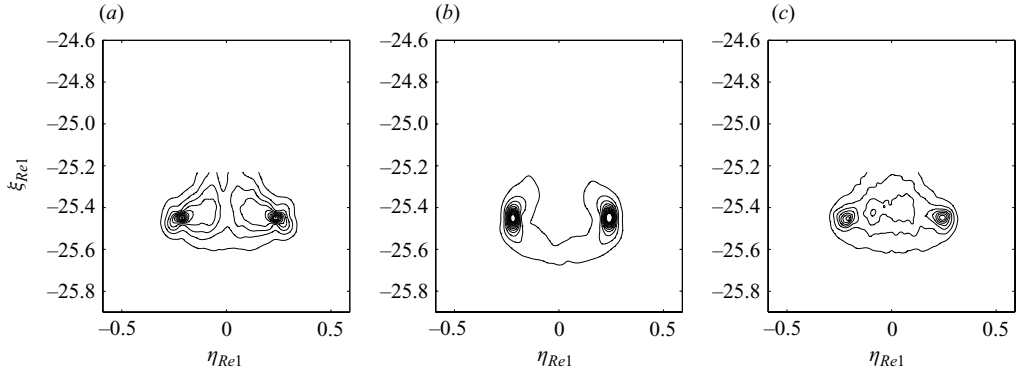


FIGURE 25. Reynolds normal stresses: $-\overline{U'U'}$, $-\overline{V'V'}$, $-\overline{W'W'}$ in similarity coordinates. Contour levels are −12.0(1.0)0.0, −24.0(2.0)0.0 and −12.0(1.0)0.0 for three components, respectively. Higher levels in the core centre area are not shown.

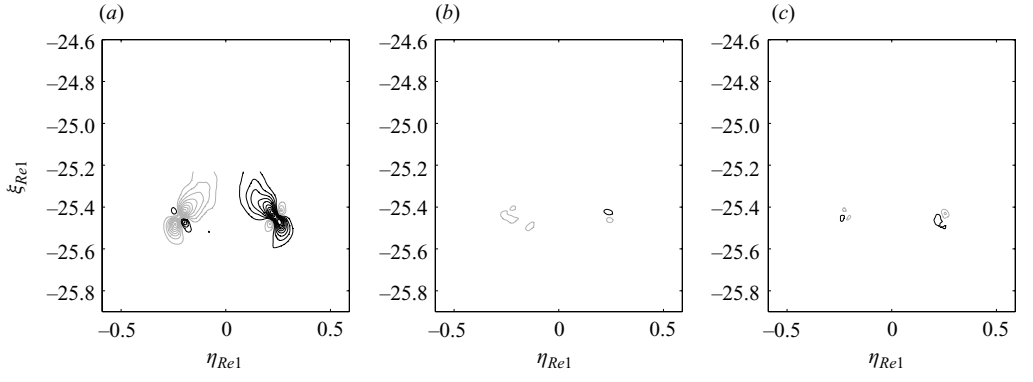


FIGURE 26. Reynolds shear stresses: $-\overline{U'V'}$, $-\overline{U'W'}$, $-\overline{V'W'}$ in similarity coordinates. Contour level is −4.5(0.5)4.5. Higher levels in the core centre area are not shown.

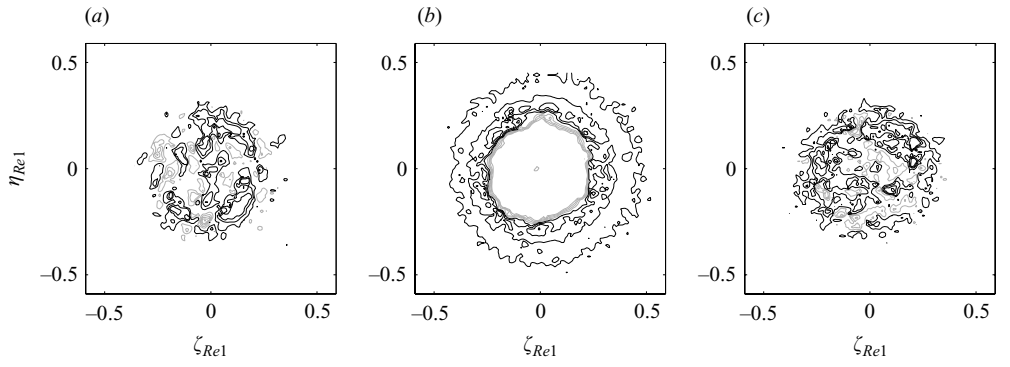


FIGURE 27. Instantaneous velocity contours in azimuthal plane presented in similarity coordinates when the PIV plane approximately cuts through the ring core. (*a–c*) $U$, $V$, $W$; the symbol assignment is consistent with the two-dimensional results. Contour levels are −8.0(2.0)8.0, −16.0(2.0)4.0, −8.0(2.0)8.0, 0 level bypassed. The PIV plane of two-dimensional or first stereoscopic set-up is along $\eta$ direction. Note that $U$, $V$, $W$ are in Cartesian coordinates.

$\tau$ into several possible contributions. This section attempts only to quantify the contribution of dispersion to the turbulence quantities. The authors do not claim that the 'corrected' quantities are accurate, because that would require fully three-dimensional data over a volume:

$$\tau_{total} = \tau^{(1)}_{position} + \tau^{(2)}_{radius+tilt} + \tau^{(3)}_{intensity} + \tau^{(4)}_{shape}, \tag{3.5}$$

where $\tau_{total}$ represents the true stresses which are shown in figures 16–18, position, radius, tilt and shape are all apparent properties reflected by the core positions which might be due to azimuthal waves. The same equation can also be applied to the turbulence production. The $\tau_{total}$ contours are directly obtained from the experiments, including all the factors on the right-hand side of (3.5) and without any artificial correction. It now becomes possible to estimate the percentage contribution to the stresses due to these factors. In this section, mathematical processes are designed in an attempt to separate the contributions from these factors.

The easiest factor to filter out in (3.5) is (1), due to dispersion of position. In other words, the first method is designed in order to shrink the core centroids' footprints cluster at each station to one point or to bring down the curves in figure 20 to close enough to zero. At each station described in § 3.1, the left and right halves of a single ring are considered to be uncorrelated, and each half is shifted until the core centroid of the corresponding half collapses with a destination point. The destination points are chosen to be the intersections of each station line in a streamwise position and the fitting lines in figure 4. Although the core centroids of 50 realizations now collapse by applying the shifting, this process does not filter out factor (2). This is because shifting in rectangular grids does not change the ring's tilting angle in the PIV plane and it does not correct the curvature differences around the core due to the ring size difference. The result of applying this process is an overestimation of the stresses towards the centre of the ring (the centre axis). In an effort to reduce this overestimation, 20 realizations whose core centroids are closest to the destination points are used in the averaging. Figure 28 shows that this method filters out up to 30 % of the total stresses, especially for $Re_2$ case when the apparent dispersion is strong. This illustrates the effectiveness of the 'filtering' and clearly shows the size of the possible contribution of core position dispersion to the total stresses.

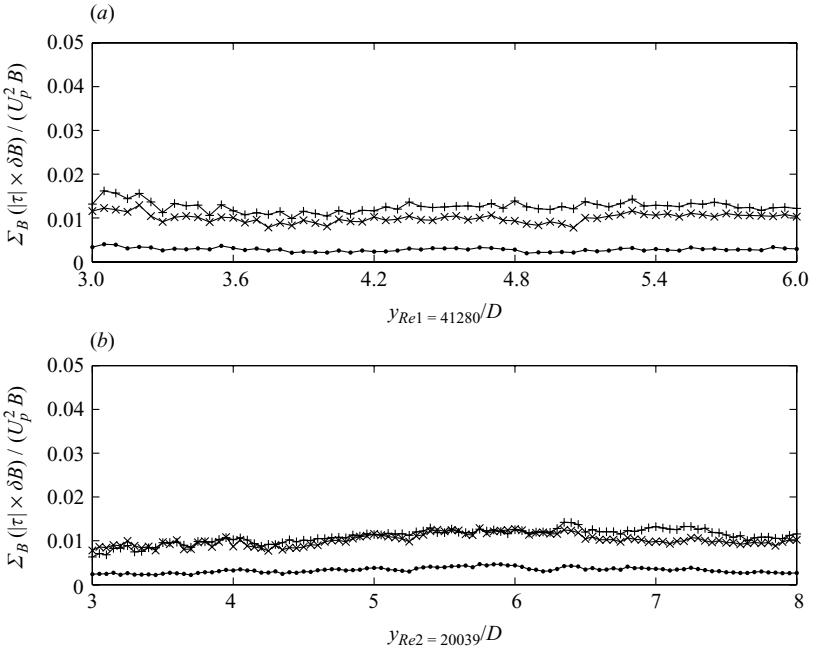


FIGURE 28. The summation of the magnitude of the three Reynolds stresses $-\overline{u'u'}$, $-\overline{v'v'}$ and $-\overline{u'v'}$ in the ring bubble area $\int_B |\tau| \, \mathrm{d}\boldsymbol{B}/U_p^2 B$ as a function of rings' streamwise locations after shifting each core centroid to the desired collapse point. $B$ is the rectangular region of $1.4D$ in the streamwise direction and $2.4D$ in the radial direction. Symbols: +, axial Reynolds normal stress; ×, radial normal Reynolds stress; ●, Reynolds shear stress.

For the purpose of subtracting factor (2) from (3.5), a technique is borrowed from the analysis of Glezer & Coles (1990) that was applied to their LDV data. Each column in the resultant data mesh (the vector field) is assumed to be uncorrelated with the neighbouring columns. The velocity mesh grid is $85 \times 85$; thus, effectively there are 85 LDV testing stations across the radial direction. A single realization from the PIV is equivalent to 85 LDV velocity traces. In this way, data at each column has no idea about what happens in the neighbouring columns. The algorithm is summarized in the following steps.

(*a*) If one column is considered, for each of the 50 rings produced, the PIV image number (at a particular time) corresponding to the minimum root mean square (r.m.s.) of velocity components with respect to the ensemble-averaged velocity components at that column is picked out. The first ensemble-averaged velocity components are calculated from the raw averaging process which is described in § 3.1. These ensemble-averaged values will be updated after the second step. This process is equivalent to the shifting process of Glezer & Coles (1990). However, instead of shifting the axial velocity component to find the minimum r.m.s. only, in this method, both axial and radial components are taken into consideration. In order to take into account small dispersion in the PIV plane, the neighbouring three columns (hence seven columns in total) are included for searching the minimum r.m.s. PIV image number (time point).

(*b*) After the first step, there are 50 velocity traces (including both axial and radial components) from 50 rings corresponding to one column station (the effective LDV station), after which these 50 r.m.s. values are further sorted to find the smallest

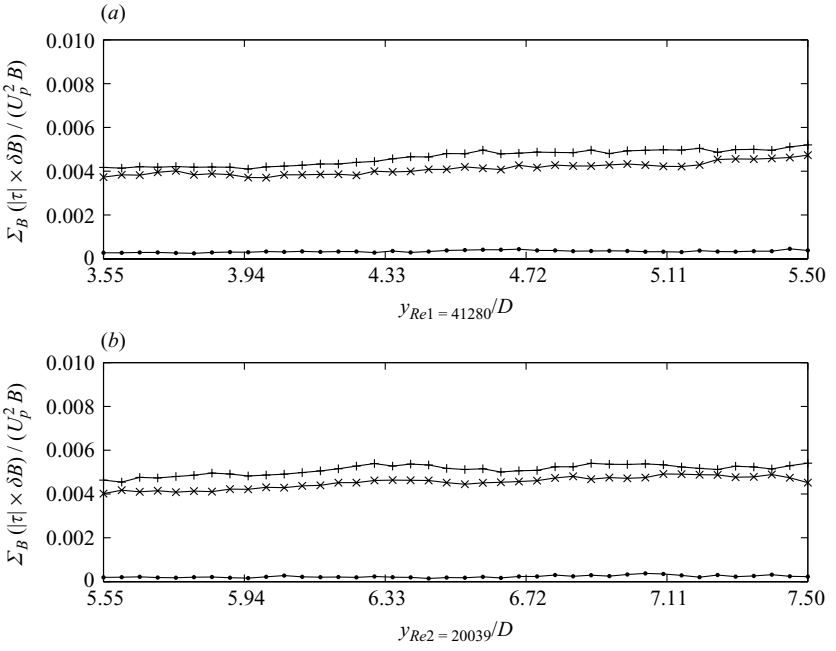


FIGURE 29. The summation of the magnitude of the three non-dimensionalized Reynolds stresses $-\overline{u'u'}$, $-\overline{v'v'}$ and $-\overline{u'v'}$ in the ring bubble area $\int_B |\tau| \, \mathrm{d}\boldsymbol{B}/U_p^2 B$ as a function of rings' streamwise locations after adopting the single-column shifting method. $B$ is the rectangular region of $1.4D$ in the streamwise direction and $2.4D$ in the radial direction. Symbols: +, axial Reynolds normal stress; ×, radial normal Reynolds stress; ●, Reynolds shear stress.

30 r.m.s. value. The final 30 traces at one column station are used to find the new ensemble-averaged velocity and the Reynolds stresses.

(*c*) The processes described above are iterated to obtain the final result for one column. The same process is applied to all the 85 columns to obtain the corrected two-dimensional stress field.

This process actually biases the velocity to a smaller value because in the first iteration it corrects the velocity components towards the raw ensemble-averaged value which has the dispersion effect included, hence has lower intensity compared with the instantaneous value of some realizations at the same relative locations, but it does not necessarily decrease the stress level. Note that, in each column, the two velocity components are correlated and they are not corrected by the circulation factor. The result is plotted in figure 29. Note that the level in figure 29 is only 20 % of that in figures 19 and 28. The stresses are also plotted in similarity scaling as shown in figure 30. It shows that stresses do not decay perfectly as the similarity theory predicts (plots are still flat in figure 29), which means that either the testing range is not long enough or factor (4) still plays a significant role which has not been subtracted. To subtract factor (4), it requires that on top of the algorithm described above, at each column the velocity traces need to be scaled to have the same standard deviation for both velocity components individually but this process would decouple the two velocity components hence has a trade off. It is for this reason that this factor is untouched. Note that the procedure used by Glezer & Coles (1990) treated the $u$ and $v$ signatures differently and separately – something they regretted at a later stage

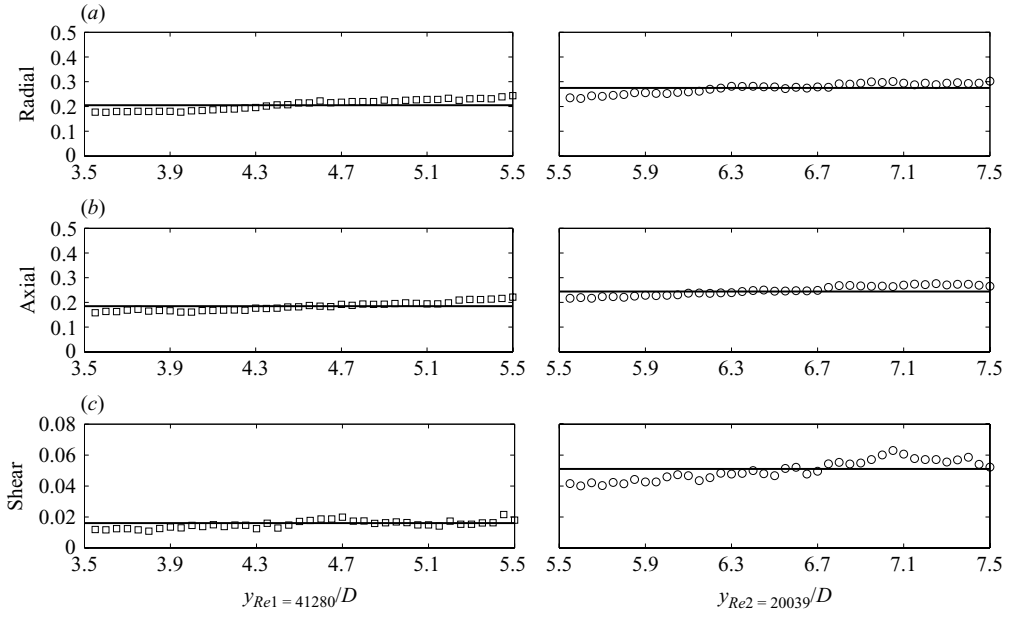


FIGURE 30. The magnitude of the non-dimensionalized Reynolds stresses in the bubble area scaled by similarity scaling law as a function of rings' streamwise locations after the second correction method is applied. Radial component $\int_B |-\overline{u'u'}|\mathrm{d}\boldsymbol{B}(\rho/I)^2(y-y_o)^4/\xi^4$; axial component $\int_B |-\overline{v'v'}|\mathrm{d}\boldsymbol{B}(\rho/I)^2(y-y_o)^4/\xi^4$; shear component $\int_B |-\overline{u'v'}|\mathrm{d}\boldsymbol{B}(\rho/I)^2(y-y_o)^4/\xi^4$. Symbols: □, $Re_1$ case; ○, $Re_2$ case; —, the zero order least square fits of $Re_1$ and $Re_2$ cases with the fixed virtual origins obtained in figure 4.

(as stated in their paper). The procedure above is then a significant improvement for this reason (and in other details).

Finally, the turbulence production level in the bubble region is plotted for the raw quantity together with the filtered quantities using the two correction methods above (see figure 31). There are a few points worth noting once more even though they are similar to those mentioned for the stress plots. Firstly, the raw levels are quite different even in dimensionless form. Like the similarity theory, the non-dimensionalizing process only accounts for the intensity but not for the dispersion; therefore, higher level in the $Re_2$ plot is reasonable (see figure 20). Secondly, after the first correction method is applied, the production levels for the two cases decrease to the level of 0.025, meaning that after the dispersion is excluded the evidence for Reynolds number independence is clear. Thirdly, as with the stress plots in figure 29, application of the second correction method reduces the level by about another 50 % and the plots are much smoother. However, if the last plots are presented in similarity scaling (see figure 32), it is noticeable that the similarity theory does not work perfectly as well, probably for the same reasons as that of the stresses.

The contours of the Reynolds stresses and the production are reproduced either after the second correction method has been applied or after factors (1) and (2) have been filtered from (3.5) (see figures 33 to 36). Although they do not precisely obey the similarity theory, they are still presented in similarity coordinates. The stress intensities in the radial and axial components are comparable now and the degree of the symmetry is increased. Because of the low-intensity range, a very weak wake appears in figure 34(*a*) but not in figure 34(*b*) nor in figure 17(*a*). The wake here is

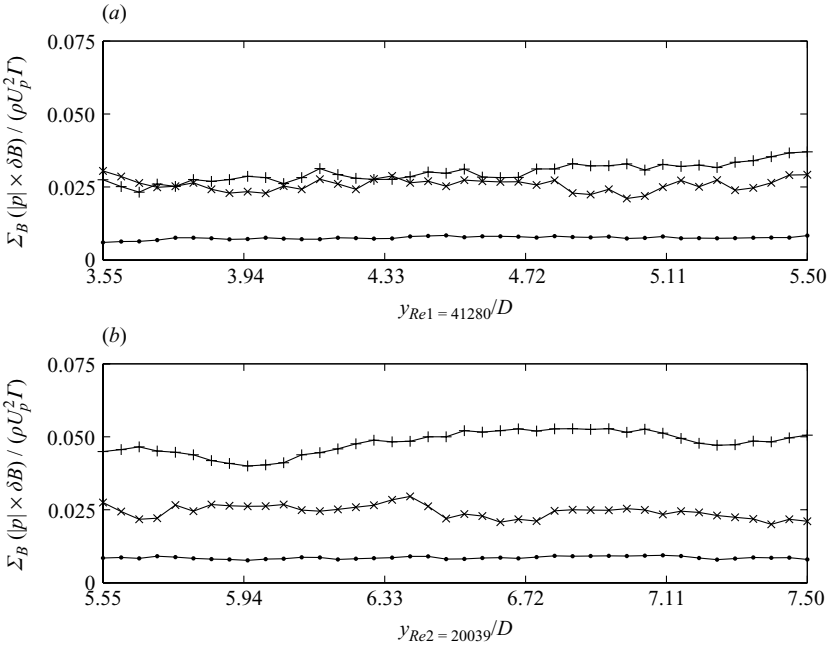


FIGURE 31. The magnitude of the non-dimensionalized turbulence production in the bubble area $\int_B |p|\, \mathrm{d}\boldsymbol{B}/\rho U_p^2 \Gamma_{slug}$ as a function of rings' streamwise locations. The production $p$ is calculated from (3.3) for $i$, $j$ up to 2. Symbols: +, the raw quantity $p_{totol}$; ×, after $p_{position}$ is filtered; ●, after $p_{position} + p_{radius+tilt}$ is filtered.

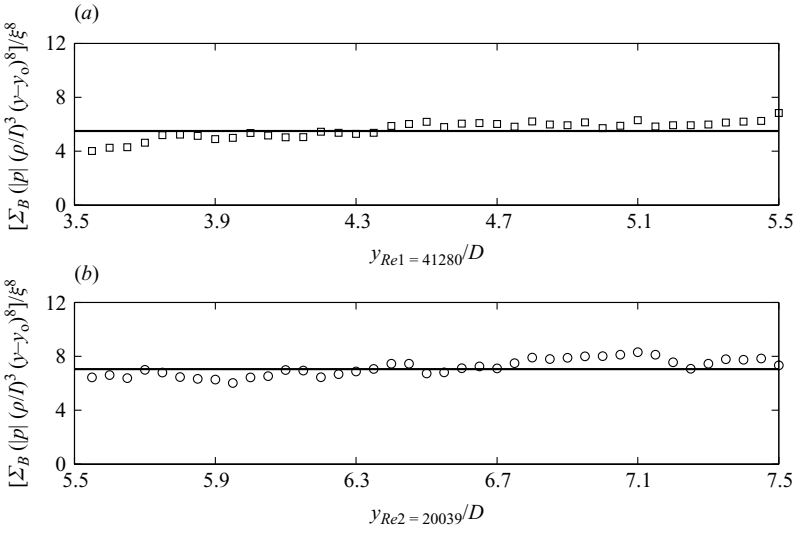


FIGURE 32. The magnitude of the non-dimensionalized turbulence production in the bubble area $\int_B |p|\, \mathrm{d}\boldsymbol{B}$ scaled by similarity scaling law $\int_B |p|\, \mathrm{d}\boldsymbol{B} (\rho/I)^3 (y - y_o)^8 / \xi^8$ as a function of rings' streamwise locations after the second correction method is applied. The production $p$ is calculated from (3.3) for $i$, $j$ up to 2. Symbols: □, $Re_1$ case; ○, $Re_2$ case; —, the first-order least-square fits of $Re_1$ and $Re_2$ cases with the fixed virtual origins obtained in figure 4.

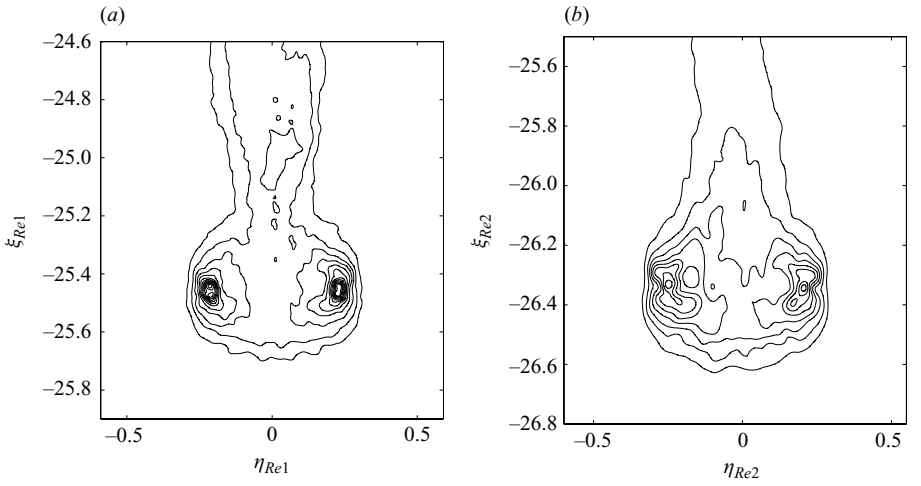


FIGURE 33. Radial normal Reynolds stresses $-\overline{U'U'}$ contour in similarity coordinates after the second correction method. Contour level is −3.6.(0.3)0.3.

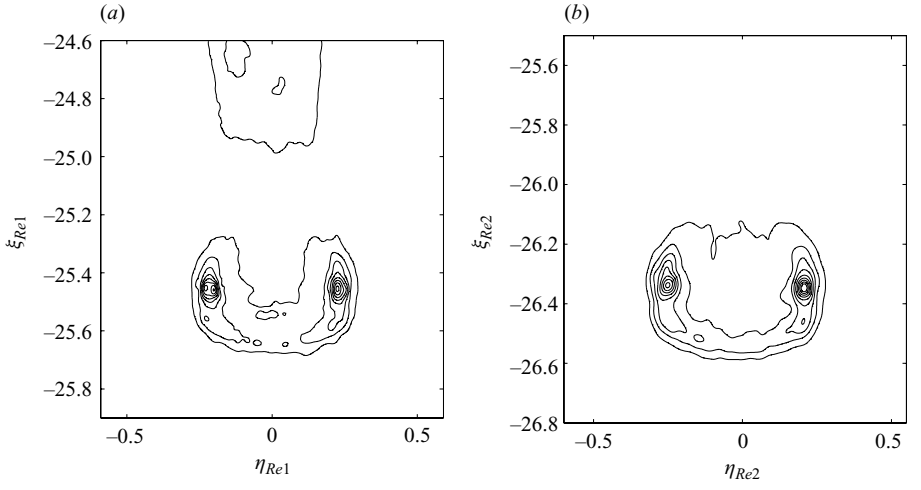


FIGURE 34. Axial normal Reynolds stresses $-\overline{V'V'}$ contour in similarity coordinates after the second correction method. Contour level is −4.5(0.5)0.5.

not the one shed from the ring structure, but the one that belongs to the formation process. This formation wake is also visible in figure 35(*a*), but it is merged with the wake shed from ring bubble. Note that with correction, the values for the quantities are very similar to those found by Glezer & Coles (1990), whereas before correction they were significantly higher. Of course, the results of Glezer & Coles (1990) were also corrected for dispersion but via a more complex procedure (which was necessary due to the fact they only had single point measurements).

## 4. Conclusions

Overall for the streamwise range considered, similarity theory seems to predict the behaviour of the circulation decay, velocity decay and growth rate quite well. In the

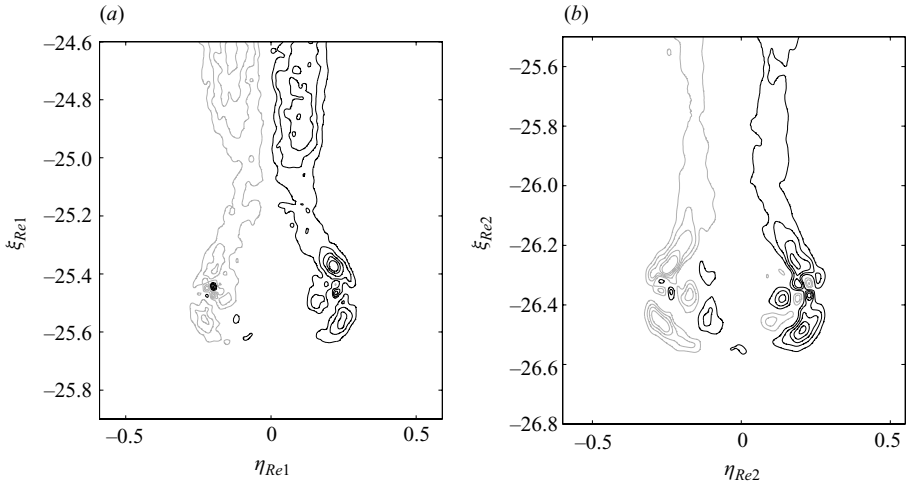


FIGURE 35. Reynolds shear stresses $-\overline{U'V'}$ contour in similarity coordinates after the second correction method. Contour level is −0.5(0.5)0.5.

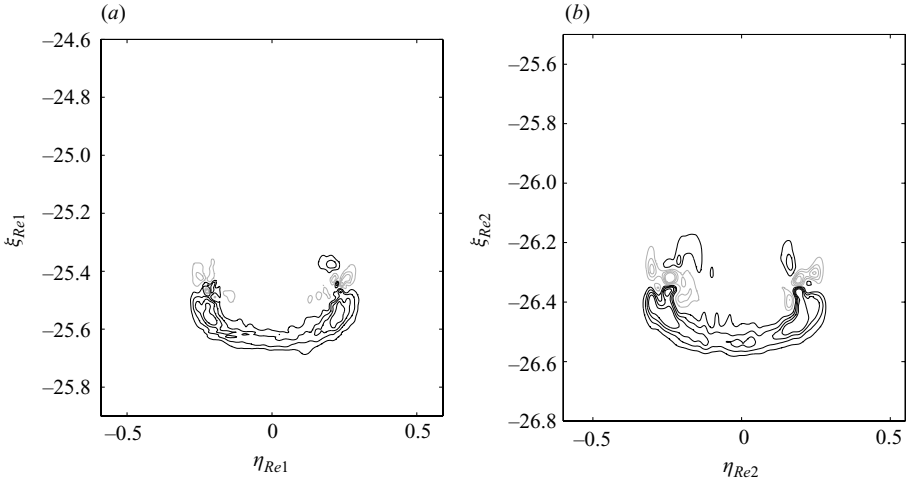


FIGURE 36. Turbulence production contour in similarity coordinates after the second correction method. Contour levels are −80(20)−20 and 20(20)80.

case of the turbulence quantities, the situation is more difficult to assess because ring dispersion has a much stronger effect on the results. After applying basic and reasonable corrections, though, it does seem that the similarity theory may apply.

The vital differences observed in these two cases, perhaps, is the degree of apparent scattering of core centroids which can be seen in figures 4 and 19. As has been emphasized, the apparent scattering is part of the nature of turbulent rings due to azimuthal waves and because the waves travel in the azimuthal direction, the PIV plane can cut at local peak or valley of the waves and not necessarily in a totally random fashion. In other words, there could be a trend that at a certain streamwise location, waves rotate at azimuthal angles such that on one side, cores appear more scattered than on the other. (Of course, the imperfection of the ring generator could be another possibility, although it is believed to be a minor factor.) This could also

| Figure | Quantity on vertical axis | Similarity quantity | $(Re_1)$ | $(Re_2)$ | LDV |
|---|---|---|---|---|---|
| 6 | $\left[4u_t\,(\rho/I)\,(y-y_o)^3\right]^{1/4}$ | $\xi$ | 25.587 | 26.500 | 25.0 |
| 6 | | $U_t$ | 6.40 | 6.63 | 6.25 |
| 4 | | $\eta$ | 0.225 | 0.232 | |
| 5* | $v_{peak}\,(\rho/I)\,(y-y_o)^3/\xi^3$ | $V_{peak}$ | 15.464 | 15.177 | |
| 9* | $\left[\int_{B'}\omega\,\mathrm{d}x\mathrm{d}y\right](\rho/I)\,(y-y_o)^2/\xi^2$ | $\int_{S'}\widehat{\omega}\,d\xi\,\mathrm{d}\eta$ | 6.869 | 7.096 | 7.71 |
| 7 | $\left[\int_{y_a}^{y_b}\pi x^2\,\mathrm{d}y\right]\xi^3/(y-y_o)^3$ | $\int_{\xi_a}^{\xi_b}\pi\eta^2\,\mathrm{d}\xi$ | 0.076 | 0.078 | 0.048 |
| 30* | $\int_B\lvert-\overline{u'u'}\rvert\mathrm{d}\boldsymbol{B}(\rho/I)^2\,(y-y_o)^4/\xi^4$ | $\int_S\lvert\overline{U'U'}\rvert\mathrm{d}\xi\,\mathrm{d}\eta$ | 0.205 | 0.275 | |
| 30* | $\int_B\lvert-\overline{v'v'}\rvert\mathrm{d}\boldsymbol{B}(\rho/I)^2\,(y-y_o)^4/\xi^4$ | $\int_S\lvert\overline{V'V'}\rvert\mathrm{d}\xi\,\mathrm{d}\eta$ | 0.185 | 0.244 | |
| 30* | $\int_B\lvert-\overline{u'v'}\rvert\mathrm{d}\boldsymbol{B}(\rho/I)^2\,(y-y_o)^4/\xi^4$ | $\int_S\lvert\overline{U'V'}\rvert\mathrm{d}\xi\,\mathrm{d}\eta$ | 0.016 | 0.051 | |
| 32* | $\int_B\lvert p\rvert\,\mathrm{d}\boldsymbol{B}(\rho/I)^3\,(y-y_o)^8/\xi^8$ | $\int_S\lvert P\rvert\mathrm{d}\xi\,\mathrm{d}\eta$ | 5.50 | 7.05 | |

TABLE 1. Similarity constants obtained from the plots. LDV represents the results from Glezer & Coles (1990). Here $U_t$ is the similarity quantity corresponding to the ring navigation velocity, $U_t = u_t\,(\rho/I)^{1/4}\,(t-t_o)^{3/4} = (1/4)\xi$. The asterisk (*) denotes that the plots do not obey the similarity theory perfectly but the least-square fitting is still applied to find the similarity quantities. Note that $\widehat{\omega}$ is the dimensionless vorticity; $B$ is the bubble region in real coordinates; $B'$ represents half of the bubble region for circulation calculation in real coordinates; $S$ is the bubble region in similarity coordinates; $S'$ represents half of the bubble region for circulation calculation in similarity coordinates. $P$ is the dimensionless turbulence production calculated from the first four terms in (3.4). Note that in the circulation item, LDV results are computed for the full flow field; however, figure 9 shows that the full field circulation deviates from the similarity theory significantly. The circulations shown here hence are the bubble circulations.

be a reason why in the $Re_2$ case in figure 20, the two curves split at about $y/D = 5.5$ and soon after $y/D = 7$ they merge again. (Note that 50 realizations should guarantee convergence; see figure 3.) The amplitude of the waves directly relates to the degree of instability which is a function of rings' propagation time and distance. The detailed investigation of this scattering trend is left for future study.

When quantities are plotted to verify the similarity theory, they are scaled with the virtual origins fixed and the zero order least square fits are applied. If the similarity theory works, the plots should follow the fitting lines. The fitting of the plots is very sensitive to the locations of the origins, which are obtained from figure 4. The $Re_2$ case in figure 4 is more scattered, it makes sense to imagine that if the outer part of the individual traces is used to fit (By using the outer part, the authors are suggesting that the inner parts do not reveal the true ring radius, they are rather influenced either by the azimuthal waves or by the dispersion.), a nearer origin may be obtained which changes the plots slightly and leads to better fits in some figures, like in figure 5.

The results presented have shown that all the ensemble-averaged quantities measured in this experiment are not strong functions of Reynolds number when the rings are produced as turbulent and at least up to $Re = 41\,280$, although the turbulence quantities, after correction, still indicate slightly different similarity quantities. Therefore, the elimination of $\nu$ in (2.2) is a reasonable assumption. Although the hydrodynamic impulse of the entire flow field, after some computational error is excluded as described in § 3.1, drops, the drop is not significant at least for the first few orifice diameters (see figure 10); furthermore, since the similarity theory works for the ring bubble area, it makes sense to consider the ring bubble impulse instead

of the full field impulse, and this quantity is fairly constant. The vortical structure shedding as observed by Maxworthy (1974) does not involve significant impulse shedding. When all the assumptions work, similarity theory predicts the development of single-point properties only, e.g. $\tau$ and $p$. When the ensemble-averaging process is applied to obtain these quantities, to properly verify the theory requires that all the realizations are ideal in the sense that they are of the same location, size, tilting angle and shape. This is not possible because of the effect of (apparent) core dispersion, which is inherent in the nature of turbulent vortex rings and it is the (apparent) core dispersion that has a significant effect on the results. The contribution from the intensity fluctuation is believed to be below 10 % of the raw or total level and because the shapes of the turbulent vortex rings are difficult to adjust to be the same, perfect similarity decay is not seen. Despite the imperfection in the similarity decay, they are least square fitted to give the values and from which similarity quantities are presented in table 1.

## REFERENCES


Dabiri, J. O. 2009 Optimal vortex formation as a unifying principle in biological propulsion. *Annu. Rev. Fluid Mech.* **41**, 17–33.

Dabiri, J. O. & Gharib, M. 2004 Fluid entrainment by isolated vortex rings. *J. Fluid Mech.* **511**, 311–331.

Didden, N. 1979 On the formation of vortex rings: rolling-up and production of circulation. *Z. Angew. Math. Phys.* **30**, 101–116.

Gharib, M., Rambod, E. & Sharrif, K. 1998 A universal time scale for vortex ring formation. *J. Fluid Mech.* **360**, 121–140.

Glezer, A. 1988 On the formation of vortex rings. *Phys. Fluids* **31**, 3532–3542.

Glezer, A. & Coles, D. 1990 An experimental study of turbulent vortex ring. *J. Fluid Mech.* **211**, 243–283.

Johnson, G. M. 1971 An empirical model of turbulent vortex rings. *AIAA J.* **9**, 763–764.

Krueger, P. S. & Gharib, M. 2003 The significance of vortex formation to the impulse and thrust of a starting jet. *Phys. Fluids* **15**, 1271–1281.

Lim, T. T. & Nickels, T. B. 1995 Vortex rings. In *Fluid Vortices* (ed. S. I. Green). Kluwer.

Maxworthy, T. 1974 Turbulent vortex rings. *J. Fluid Mech.* **64**, 227–239.

Maxworthy, T. 1977 Some experimental studies of vortex rings. *J. Fluid Mech.* **81**, 465–495.

Saffman, P. G. 1992 *Vortex Dynamics*. Cambridge University Press.

Sallet, D. W. & Widmayer, R. S. 1974 Sekundärwirbelbildung bei Ringwirbeln und in Freistrahlen. *Z. Flugwiss. Weltraumforsch* **4**, 307–318.

Shariff, K. & Leonard, A. 1992 Vortex rings. *Annu. Rev. Fluid Mech.* **24**, 235–279.

Weigand, A. & Gharib, M. 1994 On the decay of a turbulent vortex ring. *Phys Fluids* **6** (12), 3806–3808.

Widnall, S. E. & Tsai, C. Y. 1977 The instability of the thin vortex ring of constant vorticity. *Phil. Trans. R. Soc. Lond.* A **287**, 273–305.